

Article

Skill and Intercomparison of Global Climate Models in Simulating Wind Speed, and Future Changes in Wind Speed over South Asian Domain

Naresh K. G. Lakku * and Manasa R. Behera

Department of Civil Engineering, Indian Institute of Technology Bombay, Mumbai 400 076, Maharashtra, India; manasa.rb@iitb.ac.in

* Correspondence: 194044004@iitb.ac.in; Tel.: +91-90-3223-9184

Abstract: Investigating the role of complex dynamical components of a global climate model (GCM) in improving near-surface wind speed (WS) simulation is vital for the climate community in building reliable future WS projections. The relative skill of GCMs in representing WS at diverse climate variable scales (daily, monthly, seasonal, and annual) over land and ocean areas of the South Asian domain is not clear yet. With this in mind, this paper evaluated the skill of 28 Coupled Model Intercomparison Project phase five GCMs in reproducing the WS using a devised relative score approach. It is recommended to use the mean ensemble of MPI-ESM-MR, CSIRO-Mk3.6.0, and GFDL-ESM2G GCMs for understanding future changes in wind-wave climate and offshore wind energy potential. The inter-comparison of GCMs shows that the GCM with high or low atmospheric resolution does not necessarily exhibit the best or worst performance, respectively, whereas the dynamic components in the model configuration play the major role, especially the atmosphere component relative to other dynamical components. The strengthening of annual and seasonal mean WS is observed over coastal plains of the United Republic of Tanzania, Oman, eastern Thailand, eastern Gulf of Thailand and Sumatra, and weakening over the central northern equatorial region of the Indian Ocean in the 21st century for RCP4.5 and RCP8.5 emission scenarios.

Keywords: near-surface wind speed; relative score; CMIP; GCM; South Asian domain



Citation: Lakku, N.K.G.; Behera, M.R. Skill and Intercomparison of Global Climate Models in Simulating Wind Speed, and Future Changes in Wind Speed over South Asian Domain.

Atmosphere **2022**, *13*, 864. <https://doi.org/10.3390/atmos13060864>

Academic Editor: Massimiliano Burlando

Received: 29 March 2022

Accepted: 20 May 2022

Published: 25 May 2022

Publisher's Note: MDPI stays neutral with regard to jurisdictional claims in published maps and institutional affiliations.



Copyright: © 2022 by the authors. Licensee MDPI, Basel, Switzerland. This article is an open access article distributed under the terms and conditions of the Creative Commons Attribution (CC BY) license (<https://creativecommons.org/licenses/by/4.0/>).

1. Introduction

Climate change due to an increase in greenhouse gases has a direct impact on atmospheric circulation, where the wind is one of the important atmospheric variables that can significantly affect evapotranspiration, wind energy, and wind-generated ocean waves [1]. The changes in wave climate make coasts vulnerable to erosion/accretion. The present wave climate is already affected by climate change; it is expected that by the end of 2060, sixty percent of the global ocean will be affected by climate change [2]. Developing nations are most vulnerable to damage caused by climate-induced disasters, as per Wallemacq et al. [3]; climate-related and geophysical disasters killed 1.3 million people and left a further 4.4 billion injured, homeless, displaced, or in need of emergency assistance. The development of the renewable energy sector and novel approaches to adaptation and mitigation strategies over a vulnerable region to counteract climate change require a proper understanding of future climate change.

Historical and future wind projections are available from several numerical climate models, which are mathematical representations of the earth's climate system and helps us to study how this earth's climate system as a whole is likely to respond to future changes in energy flows. The global climate models (GCMs) represent the climate system on a global scale, and the regional-scale climate variable statistics derived from outputs of GCMs may or not be the same as predicted statistics at a global level. The climate

variable data for regional level impact studies can be derived by dynamical downscaling [4–6] and statistical downscaling [7–9]. Although several climate model outputs are available to the research community, the incomplete knowledge of the climate physics, simplification/approximation of various numerical schemes, and parameterization of climate processes that exist at finer spatial resolution lead to inevitable bias and model uncertainty [10,11]. A recent study by Morim et al. [12] highlights that the uncertainty in inter-model GCMs surface winds is significant and cannot be neglected. Researchers have used bias correction techniques to minimize the climate model systematic bias, and to reduce model uncertainty it is recommended to run an ensemble of models to summarize the multiple climate projections from different models with the same scenario [10,13–15]. Most of the studies [15–22] investigated the wind climate and wind-generated ocean wave climate variability using an ensemble of climate models, with or without evaluation of available all individual models' competence. Few studies [21,22] reported that an ensemble of the best-performing models outperformed an ensemble of all models. However, they failed to address the quantitative criteria for selecting climate models as part of an ensemble. A brief review of skill indicators used for assessing the skill of climate models are well presented by Raju and Kumar [23]. They observed that most studies failed to report the basis of selecting a particular indicator, simple methodology to collate the different skill indicator metrics to a single score to rank GCMs, and technique to select the subset of GCMs as part of the ensemble. Further studies [24,25] show that constructed best performing GCM is sensitive to the chosen decision technique, the number of skill indicators considered, and the variable of interest. In the light of the above literature, the current study devised a comprehensive score-based method for constructing the best-performing climate model in simulating wind speed.

The skill of CMIP5 GCMs in simulating rainfall [26,27], temperature [28,29], and sea level pressure [30] has been widely examined. Notable studies [15,21,22,31–33] have investigated the skill of GCMs in representing near-surface wind speed over the ocean areas of the South Asia (SA) domain, but the skill of GCMs over land of the SA domain needs to be investigated further. The skill of GCMs over land may differ from the ocean due to complex and different topography over continents. The onshore wind farm locations and layout will depend on the available wind potential and its possible changes in future. This requires assessing the skill of climate models over land. A study by Mohan and Bhaskaran [21] evaluated the performance of CMIP5 climate models relative to satellite altimetry data in representing monthly mean wind speed for a period from 2006 to 2016 over the Indian Ocean (IO) using Taylor's skill score and selected the 10 best performing models. It was found that the model constructed from an ensemble mean of top ten performing models performed better than an individual model. In general, GCMs are good at representing long temporal scale mean climate compared to shorter temporal scales, and most structural designs and climatic change studies require approximately 30 years of data [7]. Further, Morim et al. [12] show that inter-model uncertainty is two to four times greater than the uncertainty associated with model internal variability, and assessing the skill of particular aspects of wind climatology might mislead the performance of GCM. Therefore, Mohan and Bhaskaran [21] study results can be improved by evaluating the GCMs' skill over different climate variable scales (daily, seasonal, and annual) and by increasing the study period to approximately 30 years. Krishnan and Bhaskaran [22] evaluated the skill of CMIP5 and CMIP6 GCMs in simulating near-surface wind speed; however, their study was limited to the Bay of Bengal (BoB). Kulkarni et al. [15] evaluated the skill of 10 CMIP5 GCMs along with a multi-model ensemble mean of 10 GCMs (MME) and found that the MME based results on wind extremes and wind potential at the Indian offshore region were more consistent with Climate Forecast System Reanalysis (CFSR) data than individual GCMs for the period 1979–2005. The above study results are based on a small number of GCMs and are confined to the Indian offshore region; nevertheless, there is a potential that including GCMs and assessing over the entire Indian Ocean offshore regions can reduce model-based uncertainty. Barthelmie and Pryor [34] show that it is possible to limit the greenhouse gas

emissions to avoid the 2 °C warming threshold by increasing the potential contribution of wind energy in supplying 10–31% of electricity worldwide by 2050. Renewable energy sources, particularly wind energy, are abundant in the South Asian area. As of September 2018, 34,605 MW capacity wind power facilities had been installed in India, making it the second-largest wind market in Asia after China [35]. The Somali waters, Arabian Sea, and southern part of North Indian Ocean were identified as the most energy-rich areas (wind energy density 350–650 W/m², wave energy density 9–24 KW/m) by analyzing wind and wave climate for the period 2008–2017 [36]. With proper planning, we can use these natural resources to close the energy gap and avert a future energy crisis [37]. A reliable and best way to study the future wave climate is by using future wind as a driving force in numerical wave models to simulate future ocean waves [5–7]. This requires a reliable wind speed projection to develop the wind energy sector as climate change mitigation. Hence, in this study, the skill of CMIP5 GCMs in reproducing the near-surface wind speed (WS) over ocean and land are assessed separately. The Indian Ocean has a unique weather system with three different monsoon seasons: pre-monsoon (February–May), monsoon (June–September), and post-monsoon (October–January). The wind climate over the Arabian Sea (AS) is dynamic throughout the year with southwest monsoon, northeast monsoon, and shamal winds [38–41], and resulted in stronger wind and wave climate over the AS compared to BoB and equatorial region of North Indian Ocean (NIO) [39]. The monsoon winds account for most of the variance in wind field over IO [41]. During monsoon, 30% of the wind speed over AS is greater than 10 m/s and whereas it accounts for just 14% in the BoB [40]. Kumar et al. [42] observed that, the average trend of annual mean wind speed in shelf seas around India is positive (~1.67 cm/s/yr for western shelf seas and ~0.93 cm/s/yr for eastern shelf seas); however, a negative trend is observed at some locations based on ERA-I data from 1998 to 2012. Globally, the maximum rate of increase in near-surface wind speed is observed between 1991 and 2007 compared to the rate of increase for the period 1988–2011 [43]. El Nino–Southern Oscillation (ENSO) has significant impacts on the global climate and it accounts for the major skill source of seasonal-to-inter-annual climate prediction [44]. As the global climate warms up, the ENSO and sea surface temperature (SST) exhibit different characteristics. The changes in wind speed climate over the Indian Ocean region are greatly influenced by local SST and remote ENSO indices [45]. Under the context of global climate change, it is important to investigate the possible changes in future wind speed over the ocean and land of the South Asian domain.

It is observed from the literature that accurate wind speed is significant for assessing future changes in wind speed and is a vital driving component in the wave model, hydrological model, and ocean model. A detailed study over the South Asian domain considering all available CMIP5 GCMs, assessing their skill in different climate variable scales (daily, monthly, seasonal, and annual scale) over a longer (approximately 30 years) study period is essential to reduce the model uncertainty. It is imperative for end-users of the climate community to have information about the performance of climate models to estimate the impact of climate change on wind-driven processes. At the same time, it is crucial to acknowledge the benefits of increasing the complexity of a climate model by including additional dynamical components (atmosphere, land, ocean, sea-ice, carbon-cycle, and biogeochemistry) in improving the wind speed simulations. Thus, the current study compared climate models from the same family that differed in their dynamical components to better understand the role of different dynamical components in enhancing wind speed modelling. As noted earlier, different evaluation methods have been used to evaluate the climate model's skill. However, a comprehensive evaluation method is still absent to assess and suggest the best suitable climate model/ensemble of climate models in reproducing wind speed over diverse climate variable scales. Hence, a new score-based approach is presented. Further, we also examined the possible future changes in the annual and seasonal mean wind speed from top-performing climate models under the RCP4.5 and RCP8.5 scenarios.

2. Materials and Methods

This study evaluates the ability of available GCMs of the CMIP5 project to simulate the near-surface wind speed (WS) over the South Asian domain (11° S to 30° N and 26° E to 107° E, shown in Figure 1). The overall confidence in GCMs' future projections depends on their skill in representing the historical climate [46]. In order to understand how the CMIP5 GCMs represent historical and present wind climate, we used a common historical period from 1979 to 2005 and a near-present time period ranging from 2006 to 2019. These periods are selected based on GCMs and ERA5 wind field data availability.

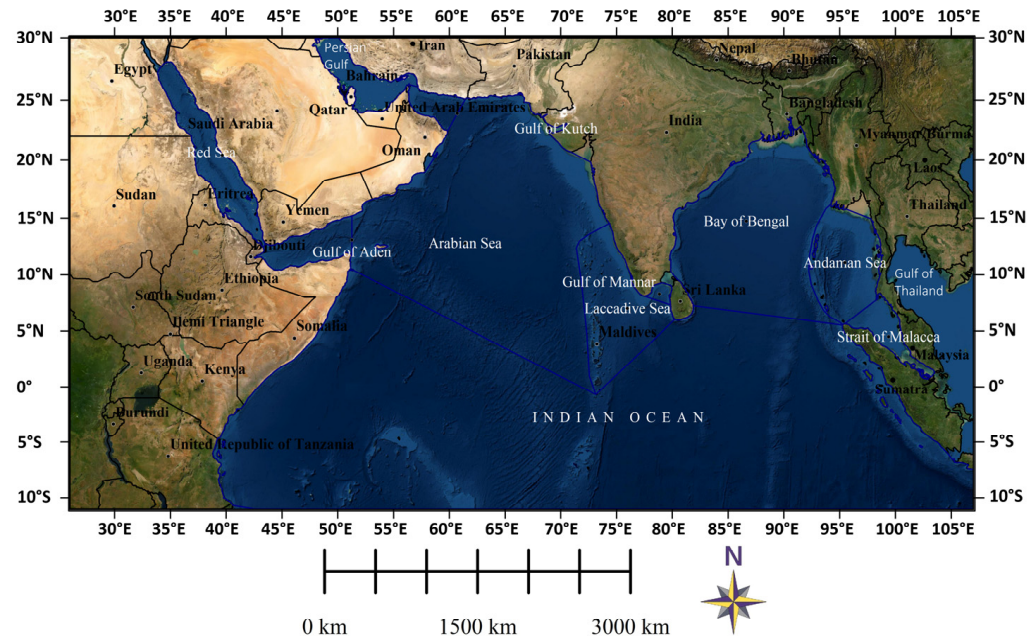


Figure 1. Study domain considered for evaluation of CMIP5 GCM's skill in representing near-surface wind speed.

2.1. Datasets

2.1.1. Model Data (CMIP5)

The GCMs of CMIP5 project simulated the WS for historical as well as for the 21st century by assuming certain scenarios called representative concentration pathways (RCPs). The daily mean zonal and meridional components of WS for twenty-eight GCMs (tabulated in Table 1 Model Id 1 to 28) were downloaded from Earth System Grid Federation (ESGF) portal (<https://esgf-node.llnl.gov/search/cmip5/>; accessed on 11 January 2021) for the historical and present time slice. Similar results are expected for all four scenarios (RCP2.6, RCP4.5, RCP6, and RCP8.5) because of similar radiative forcing in the present time slice [21], hence for this study, the moderate emission scenario RCP4.5 is considered. We considered the CMIP5 GCMs data from one realization, initial condition and model physics (r1i1p1) ensemble to study the inter-model variability.

Table 1. Attributes of CMIP5 GCMs and ERA5.

Model ID	Model Acronym	Model	Institution	Atmospheric Spatial Resolution (Latitude ° × Longitude °)
0	ERA5	Fifth-generation European Research Agency		0.25 × 0.25
1	ACCESS1.0	Australian Community Climate and Earth System Simulator	Commonwealth Scientific and Industrial Research Organisation (CSIRO), Australia, and Bureau of Meteorology (BOM), Australia	1.25 × 1.875
2	ACCESS1.3	Australian Community Climate and Earth System Simulator	Commonwealth Scientific and Industrial Research Organisation (CSIRO), Australia, and Bureau of Meteorology (BOM), Australia	1.25 × 1.875
3	BCC-CSM1.1 -M	Beijing Climate Center Climate System Model with Moderate resolution	Beijing Climate Center, China Meteorological Administration	1.1215 × 1.125
4	BNU-ESM	Beijing Normal University Earth System Model	College of Global Change and Earth System Science (GCESS), Beijing Normal University	2.7906 × 2.8125
5	CanCM4	Canadian Coupled Global Climate Model	Canadian Centre for Climate Modelling and Analysis (CCCma)	2.8125 × 2.8125
6	CanESM2	Canadian Earth System Model	Canadian Centre for Climate Modelling and Analysis (CCCma)	2.8125 × 2.8125
7	CMCC-CM	CMCC Climate Model	Centro Euro-Mediterraneo sui Cambiamenti Climatici (CMCC)	0.7484 × 0.75
8	CMCC-CMS	CMCC Climate Model with a resolved Stratosphere	Centro Euro-Mediterraneo sui Cambiamenti Climatici (CMCC)	1.8653 × 1.875
9	CNRM-CM5	CNRM coupled global climate model	Centre National de Recherches Meteorologiques and Centre Europeen de Recherche et Formation Avancees en Calcul Scientifique (CNRM-CERFACS)	1.4008 × 1.40625
10	CSIRO-Mk3.6.0	CSIRO Mark 3.6.0 model	Commonwealth Scientific and Industrial Research Organisation in collaboration with the Queensland Climate Change Centre of Excellence (CSIRO-QCCCE) Laboratory of	1.875 × 1.875
11	FGOALS-s2	Flexible Global Ocean-Atmosphere-Land System model, Spectral Version 2	Numerical Modeling for Atmospheric Sciences and Geophysical Fluid Dynamics, Institute of Atmospheric Physics, Chinese Academy of Sciences (LASG-IAP)	1.6590 × 2.8125
12	GFDL-CM3	GFDL Coupled Model version 3	Geophysical Fluid Dynamics Laboratory (GFDL)	2.0 × 2.5
13	GFDL-ESM2G	GFDL Earth System Model, an isopycnal model using the Generalized Ocean Layer Dynamics (GOLD) code base	Geophysical Fluid Dynamics Laboratory (GFDL)	2.0225 × 2.5
14	GFDL-ESM2M	GFDL Earth System Model with Modular Ocean Model 4	Geophysical Fluid Dynamics Laboratory (GFDL)	2.0225 × 2.5
15	HadGEM2-AO	Hadley Centre Global Environment Model 2 Atmosphere-Ocean	National Institute of Meteorological Research/Korea Meteorological Administration (NIMR/KMA)	1.250 × 1.875
16	HadGEM2-CC	Hadley Centre Global Environment Model 2 Carbon cycle	Met Office Hadley Centre	1.250 × 1.875
17	HadGEM2-ES	Hadley Centre Global Environment Model 2 Earth System	Met Office Hadley Centre	1.250 × 1.875
18	INM-CM4	INM Climate Model 4	Institute for Numerical Mathematics of the Russian Academy of Sciences (INM)	1.5 × 2.0
19	IPSL-CM5A-LR	IPSL Coupled Model version 5A-Low resolution	Institut Pierre-Simon Laplace (IPSL)	1.875 × 3.750
20	IPSL-CM5A-MR	IPSL Coupled Model version 5A Mid resolution	Institut Pierre-Simon Laplace (IPSL)	1.2676 × 2.500
21	IPSL-CM5B-LR	IPSL Coupled Model-version 5B new atmospheric physics at low resolution	Institut Pierre-Simon Laplace (IPSL)	1.875 × 3.750
22	MIROC4h	Model for Interdisciplinary Research on Climate version 4 with high resolution	Atmosphere and Ocean Research Institute (The University of Tokyo), National Institute for Environmental Studies, and Japan Agency for Marine-Earth Science and Technology	0.5616 × 0.5625

Table 1. Cont.

Model ID	Model Acronym	Model	Institution	Atmospheric Spatial Resolution (Latitude ° × Longitude °)
23	MIROC5	Model for Interdisciplinary Research on Climate 5	Atmosphere and Ocean Research Institute (The University of Tokyo), National Institute for Environmental Studies, and Japan Agency for Marine-Earth Science and Technology	1.4008 × 1.4063
24	MIROC-ESM	MIROC Earth System Model	Atmosphere and Ocean Research Institute (The University of Tokyo), National Institute for Environmental Studies, and Japan Agency for Marine-Earth Science and Technology	2.7906 × 2.8125
25	MIROC-ESM-CHEM	MIROC Earth System Model, atmospheric chemistry coupled version	Atmosphere and Ocean Research Institute (The University of Tokyo), National Institute for Environmental Studies, and Japan Agency for Marine-Earth Science and Technology	2.7906 × 2.8125
26	MPI-ESM-LR	MPI Earth System Model Low Resolution	Max Planck Institute for Meteorology (MPI-M)	1.875 × 1.875
27	MPI-ESM-MR	MPI Earth System Model Mixed Resolution	Max Planck Institute for Meteorology (MPI-M)	Approximately 1.875 × 1.875
28	MRI-CGCM3	MRI Coupled Atmosphere-Ocean General Circulation Model, version 3	Meteorological Research Institute (MRI)	1.12148 × 1.125
29	MME_CMIP5	Multi-Model Ensemble mean of all twenty-eight CMIP5 GCMs		0.25 × 0.25
30	MME-3_ (27, 10 and 13)	Multi-Model Ensemble mean of top 3 performed CMIP5 GCMs (Model with ID 27, 10 and 13) over ocean		0.25 × 0.25
31	MME-3_ (1, 27 and 15)	Multi-Model Ensemble mean of top 3 performed CMIP5 GCMs (Model with ID 1, 27 and 15) over land		0.25 × 0.25

2.1.2. Reference Data (ERA5)

Satellite data [47], ERA-Interim [1,19,48], ERA-40 [49], Climate Forecast System Reanalysis (CFSR) [50], and ERA5 [12,51] are the commonly used standard reference data to study and validate wind and wave climate. The in-situ observations and measurements from buoys are confined to a particular region, whereas satellite measured datasets do not have any spatial constraint, but they are not available over a long-term historical period. Due to these constraints, the performance of CMIP5 GCMs is evaluated with reference to reanalysis data. Kulkarni et al. [52] evaluated the CFSR, ERA-Interim, and NCEP WS reanalysis data over the Indian offshore region and recommend ERA-Interim among the three reanalysis datasets. In general, the choice of reference data to evaluate the model performance will depend on the availability of long-term reliable and accurate data with higher spatial and temporal resolution. In this study, the latest ERA5 wind data are used as a reference dataset, which is an improved version of its predecessor ERA-Interim. The wind data for the historical and present time slice were downloaded from the Copernicus Climate Change Service (C3S) Climate Data Store (<https://cds.climate.copernicus.eu/>; accessed on 21 January 2020) at an hourly scale having a spatial resolution of $0.25^\circ \times 0.25^\circ$. The ERA5 is assigned a model id '0' in the present study, as shown in Table 1.

2.2. Methodology

An error or bias is present in the climate model output because of incomplete knowledge/representation of various geophysical sub-processes, numerical approximations, parametrizations, and empirical formulae. A most popular method [53] and best in bias reduction among other bias correction techniques [11] named quantile mapping developed by Li et al. [54] is used for bias correction. In this method, to remove the bias we will match the cumulative distribution function (CDF) of the climate model (CMIP5 GCM) with CDF of reference (ERA5) data quantile by quantile. For doing bias correction the model WS interpolated to reference data spatial resolution of $0.25^\circ \times 0.25^\circ$ by bilinear interpolation. Here, the historical reference and model data refer to a period of 27 years from 1979 to 2005. Although the reference data are available for the present time slice (2006–2019), we consider it as a future time slice and applied the bias correction to test how close the

model's bias-corrected present projections are to reference data. In this study, the normal distribution was fitted to the daily time series of both *u* and *v* components of WS as it proved to be the best fit, and correcting the zonal and meridional components of WS will automatically correct the wind direction. From now onward, the wind field dataset of GCMs is by default the bias-corrected dataset.

2.2.1. Relative Score (RS)

The performance of models was assessed on daily, monthly, seasonal, and annual scales using a developed relative score-based approach. The relative score was computed for each assessment criteria statistic as per Equation (1), and RS varies between 0 to 1. If the model simulates the observed conditions perfectly then RS will be 1, and it will be 0 for a poorly simulated model. Table 2 lists the assessment criteria statistics (ACS) and related weighting factors used to rank the models. The final rank is assigned to each model based on total relative score (TRS), which is the summation of all individual assessment criterion RS in both time slices.

Table 2. Summary of assessment criteria statistics used for model evaluation over different climate variable scales.

Climate Variable Scale	Method/Statistic	Assessment Criteria Statistic (ACS)	W
Daily mean	Perkins Skill Score (PSS)	Bias in PSS (B_{PSS})	0.5
Spatio-temporal variability	Empirical Orthogonal Function (EOF) analysis	Empirical Orthogonal Function (EOF) analysis	1
	1. EOF1 variance;	1. Absolute Bias (AB);	
	2. EOF1 spatial and PC1 magnitude	2. Mean Absolute Bias of EOF1 (MAB_{EOF1}) and PC1 magnitudes (MAB_{PC1});	
	3. PC1 pattern;	3. 1-r;	
Annual cycle	Statistical significance of positive 'r'	P_{ir}	1
Annual mean	Statistical significance of bias	Percentage of statistically significant bias (P_b)	0
Seasonal mean			1
Annual mean trend	Mann-Kendall (MK) test Theil-Sen slope	Mean Absolute Bias of trend (MAB_{trend})	1
Seasonal mean trend			1

W = weighting factor; r = correlation coefficient; P_{ir} = percentage of statistically insignificant positive correlation coefficient.

$$Relative\ Score\ (RS_{ij}) = \frac{ACS_{j,max} - ACS_{ij}}{ACS_{j,max} - ACS_{j,min}} \quad (1)$$

$$Total\ Relative\ Score\ (TRS_i) = \sum_{j=1}^n RS_{ij} W_j \quad (2)$$

where

RS_{ij} = Relative Score of i^{th} model for j^{th} assessment criteria;

ACS_{ij} = j^{th} assessment criteria statistic value between i^{th} model and reference data;

$ACS_{j,max}$ = maximum assessment criteria statistic value for the j^{th} assessment criteria statistic;

$ACS_{j,min}$ = minimum assessment criteria statistic value for the j^{th} assessment criteria statistic;

W_j = weighting factor;

n = number of assessment criteria.

The ability of the GCM in reproducing the frequency distribution of daily mean WS is characterized by comparing the whole study domain probability distribution of GCM with the ERA5 dataset using Perkins Skill Score (PSS) [55]. The PSS is used to measure the common area between two probability density functions. It ranges from 0 to 1, where 0 indicates that there is no overlap between distributions, and 1 indicates

perfect overlap. The RS is computed for each model considering bias in PSS (B_{PSS}) as an assessment criterion statistic, which is defined as one minus PSS.

$$PSS = b_w \sum_{i=1}^n \min(f_{mi}, f_{ri}) \quad (3)$$

where n is the number of bins, b_w is the bin width, f_{mi} is the frequency density value of the model in a given i^{th} bin, and f_{ri} is the frequency density value of reference data in a given i^{th} bin.

Empirical orthogonal analysis (EOA) is carried out to characterize the spatial and temporal variability of monthly mean WS over the study domain. In this study, the first mode of EOF (EOF1), which explains a high fraction of total variance, and its corresponding principal component (PC1), which explains how this EOF1 pattern oscillates over time, are analyzed. EOF1 is obtained for each GCM and compared with ERA5. The ability of GCM in reproducing the dominant mode of monthly mean WS climate is evaluated by calculating absolute bias in the percentage of variance explained by EOF1, and to assess GCM performance in representing spatial oscillating pattern, the whole domain mean absolute bias (MAB_{EOF1}) is calculated as per Equation (4). The correlation coefficient and mean absolute bias of PC1 (MAB_{PC1}) between GCM and ERA5 are used as assessment criteria statistics to calculate RS.

$$MAB_{EOF1} = \frac{\sum_{i=1}^{n_g} \text{abs}(E_{mi} - E_{ri})}{n_g} \quad (4)$$

where n_g is the total number of grid cells, and E_{mi} and E_{ri} are the EOF1 magnitude of model and reference data at the i^{th} grid, respectively.

$$MAB_{PC1} = \frac{\sum_{i=1}^{n_m} \text{abs}(P_{mi} - P_{ri})}{n_m} \quad (5)$$

where n_m is the total number of months, and P_{mi} and P_{ri} are the PC1 magnitude of model and reference data of the i^{th} month, respectively.

The correlation coefficient was used to evaluate the ability of the GCMs to reproduce the annual cycle pattern as observed from reference data. Here the annual cycle represents the long-term monthly mean with a sample size of 12. The long-term monthly mean is calculated by averaging the monthly WS over the period of 27 years in case of the historical time slice and 14 years for the present time slice. The statistically significant positive correlation between the GCM and ERA5 was calculated using t-test at a significance level of 0.001. For each GCM, the percentage of statistically significant positive correlation (P_r) was calculated by taking the ratio of the number of statistically significant positive correlation grid points to the total number of grid points in the study domain. Finally, the percentage of statistically insignificant positive correlation coefficient ($P_{ir} = 1 - P_r$) is used as an ACS.

The annual mean and seasonal mean wind speeds are calculated for all GCMs and ERA5 at every spatial grid location of the study region. In general, the model bias is defined as modelled dataset minus referenced dataset; from this bias statistic the deviation of model dataset from reference dataset can be represented. To know whether this bias is statistically significant, the t-test was used with a significance level of 0.001. The percentage of statistically significant bias (P_b , the ratio of the number of significant bias grid points to the total number of grid points) is computed and used as an assessment criterion statistic.

The models' ability to capture the observed trend computed from the ERA5 dataset was tested. The Mann–Kendall (MK) non-parametric rank-based test [56,57] is used to identify the monotonic trend, and the Theil–Sen slope [58] is used to estimate the magnitude of the trend in annual mean and seasonal mean WS. These tests assume that the sample data are serially independent. Kulkarni and von Storch [59] showed that the existence of serial correlation led to fault trend detection using the MK test. The prewhitening technique is

used to reduce the serial correlation of time series data by introducing serially independent white noise to the original data. Yue and Wang [60] show that prewhitening can result in the removal of a portion of the trend. Wang et al. [61] recommended increasing the significance level and sample size/time series to improve the power of the MK test. Thus, in this study, the significance level of 0.1 is used without applying prewhitening. The whole domain mean absolute bias (MAB_{trend}) in trend magnitude is estimated as per Equation (6), and MAB_{trend} is used to calculate RS.

$$MAB_{trend} = \frac{\sum_{i=1}^{n_g} abs(\beta_{mi} - \beta_{ri})}{n_g} \quad (6)$$

where n_g is the total number of grid cells, and β_{mi} and β_{ri} are the model and reference trend magnitude at the i^{th} grid, respectively.

2.2.2. Percentage Change in Future Mean Wind Speed Projections

The 21st century is divided into three time slices to analyze changes in future mean wind speed climate: near-term (2020–2049), mid-term (2050–2079), and long-term (2080–2100). Although wind speed projections are available from all the GCMs for the 21st century, the reliability of future projections depends on the performance of GCMs in simulating present-day wind speed climate. As a result, the performance of all the GCMs was evaluated using the methodology presented in Section 2.2.1. The future projections from GCM with the highest TRS over ocean and land are used to investigate the changes in WS over the SA domain. By assuming the statistical properties of the systematic bias as stationary, the bias in future WS is corrected using the quantile mapping technique. The percentage change in the future mean WS relative to historical mean WS is examined on annual and seasonal scales over ocean and land for the RCP4.5 and RCP8.5 scenarios. The percentage change (Δ , %) is defined as the ratio of climate change to the ERA5 historical mean WS multiplied by 100, where climate change is the difference between GCM future and ERA5 historical mean WS.

$$\Delta (\%) = \frac{\bar{X}_{future} - \bar{X}_{historical}}{\bar{X}_{historical}} \times 100 \quad (7)$$

where \bar{X}_{future} and $\bar{X}_{historical}$ are the mean wind speed corresponding to future and historical time slices.

3. Results and Discussion

To reduce model uncertainty, Tebaldi and Knutti [10] recommended using a multi-model ensemble. Therefore, along with each individual model, the ensemble mean of twenty-eight CMIP5 GCMs (MME_CMIP5) and ensemble mean of 'n' top-performing models (MME-n) performance is examined, and the results are as follows.

3.1. Skill of CMIP5 GCMs in Reproducing Wind Speed Climate

The models' skill at different climatic variable scales is addressed based on estimated ACS for the ocean and land areas of the SA domain as well as the entire domain for both study time slices. The smaller the ACS value, the better the model performance.

3.1.1. Daily Mean Wind Speed

All the individual models performed well over ocean and land with at least an overlap of 92% (Figure 2). This is expected because the bias in the models was corrected quantile by quantile. Hence, the weighting factor of 0.5 is used to compute the Total Relative Score. The MME_CMIP5 has the highest ACS over ocean and land due to the average effect of finding ensemble mean WS from all models.

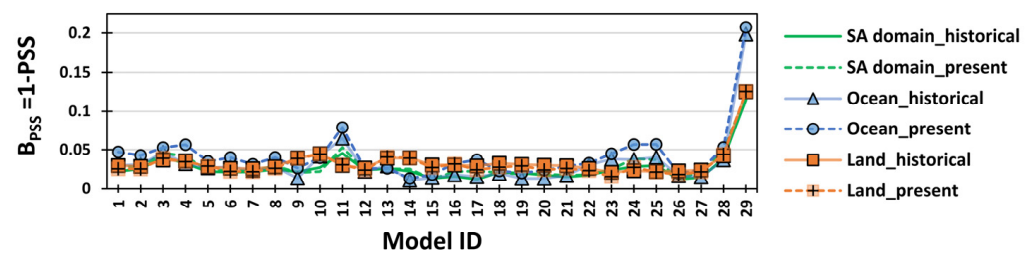


Figure 2. Assessment criteria statistic (ASC) of CMIP5 GCMs summary in reproducing frequency distribution of daily mean wind speed over South Asian (SA) domain for historical period (1979–2005) (green solid line), over SA domain for present period (2006–2019) (green dashed line), over ocean for historical period (blue solid line with triangle markers), over ocean for present period (blue dashed line with circle markers), over land for the historical period (orange solid line with plus sign markers), and over land for present period (orange dash line with square markers); ASC (bias in Perkins Skill Score (B_{PSS})) on y-axis and Model ID on x-axis.

3.1.2. Spatio-Temporal Variability

We carried out the EOF analysis to evaluate the models' ability in capturing the observed spatio-temporal variability of monthly mean WS. The ERA5 historical monthly mean WS EOF1 accounts for 65.19% of the total variance and shows maximum variability in WS along the flow of Somali Jet (Refer to Figure 3a). Therefore, the dominant mode of variability over the IO is monsoon. A similar type of pattern was observed by Anoop et al. [41], where the author carried EOF analysis on ERA-Interim monthly averaged WS from 1979 to 2012. The PC1 of ERA5 represents seasonal variation (scaled to be between -1 to 1) with an approximate time window of 4 months (Refer to Figure 3b). The monsoon scale anomalies are greater than the remaining two seasons, and pre-monsoon scale anomalies are more than for post-monsoon. The ACS summary of each GCM is shown in Figure 3c–f. The model's ACS is almost same in both time slices and it is less over land compared to the ocean. Most of the models have absolute bias below 5% in representing the percentage of variation, whereas model 5 has a maximum of 16.43% over ocean in the present time slice. Overall, models 15 and 17 show higher skill in capturing spatio-temporal variability of monthly WS over ocean and land. Even though MME_CMIP5 overestimates the EOF1 variance (9.59% and 10.62% in historical and present time slices, respectively), it is very good at reproducing the EOF1 pattern, PC1 pattern, and magnitude when compared to all individual models. Overall, the MME_CMIP5 performs well in capturing the spatial and temporal variability of monthly mean WS near to top-performing model 15. The models with id 11, 21, 2, 4, 24, 28, 5, 18, and 25 show very poor skill over the ocean, whereas models 24, 5, and 25 show poor skill over land. Mohan and Bhaskaran [21] evaluated the skill of CMIP5 GCMs in representing monthly mean WS climate over IO using the Taylor skill score and recommended the ten best performing models. Seven out of ten models (Models 15, 17, 27, 16, 8, 1, and 6) are in the top fifteen performing models in representing spatio-temporal variability of monthly mean WS over ocean. Although models 24 and 28 are also identified as best performing models as per Mohan and Bhaskaran [21], they show poor skill over ocean.

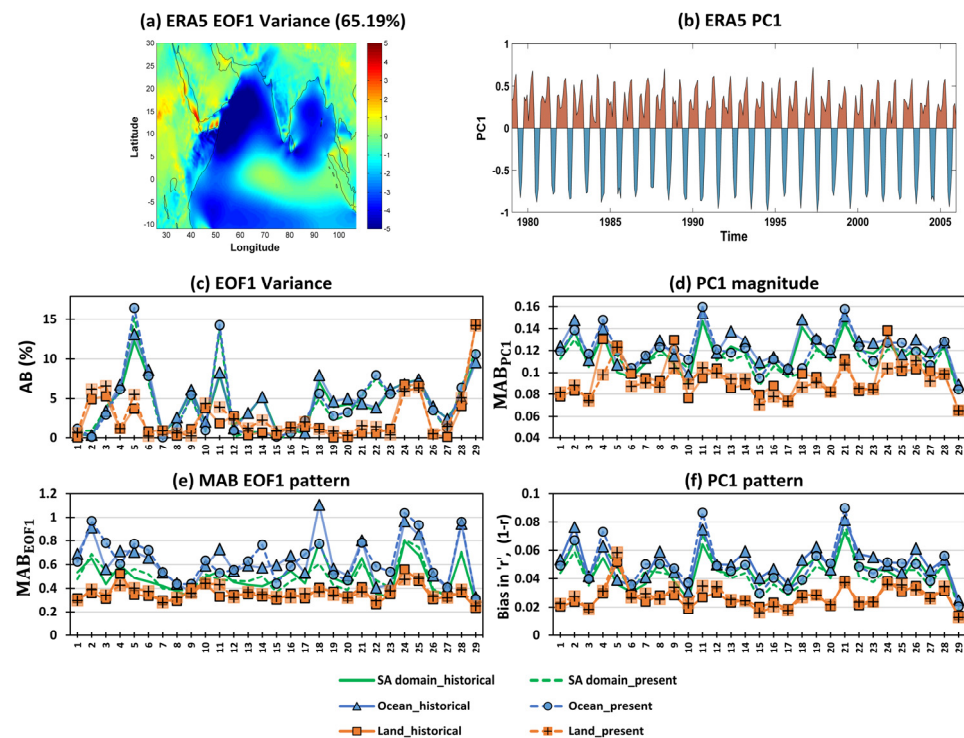


Figure 3. (a) The first mode of ERA5 historical monthly mean wind speed EOF, (b) first principal component (PC1) of ERA5 historical monthly mean wind speed EOF1. (c–f) As in Figure 2, but represents Assessment Criterion Statistic (ASC) summary of all climate models in representing the spatio-temporal variability of monthly mean wind speed; ACS (AB = absolute bias; MAB = mean absolute bias, r = correlation coefficient) on y-axis and Model ID on x-axis.

3.1.3. Annual Cycle

The overall study domain correlation coefficient ranges from 0.65 to 0.9. All the models show higher P_{ir} over the land compared to the ocean in capturing annual cycle variation (as shown in Figure 4). The P_{ir} is the same in both study time slices. Over IO, models 26 and 27 performed well with the lowest P_{ir} . Over land, models 29 and 9 have higher skill in capturing annual cycle variation. Models 24 and 25 show lower skill in capturing annual cycle variation over both ocean and land.

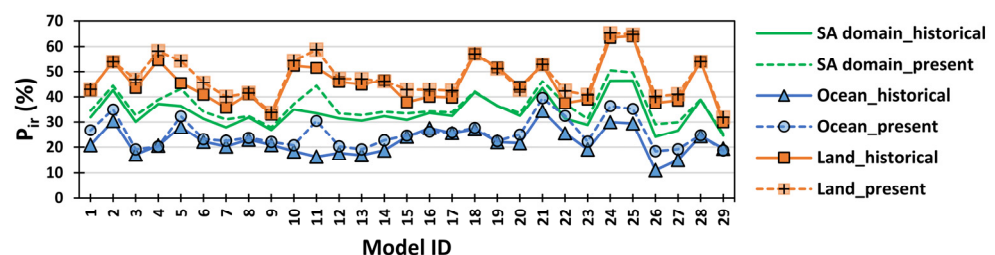


Figure 4. As in Figure 2, but summaries of the climate model's skill in capturing annual cycle pattern; the percentage of statistically insignificant positive correlation coefficient (P_{ir} , %) is on the y-axis and Model ID is on the x-axis.

3.1.4. Seasonal Mean Wind Speed

The ability of GCMs in reproducing the seasonal mean wind speed is evaluated and discussed in this section. The reference ERA5 mean WS map for both study time slices, the percentage change of present mean WS relative to historical mean WS, and the ACS summary of each GCM are shown in Figure 5. A similar mean WS pattern is observed over both time slices in three seasons. In all seasons, the mean WS is higher over IO compared to

land. Higher percentage of statistically significant bias (P_b) is observed over land compared to the ocean in all three seasons, and P_b is higher in the historical time slice.

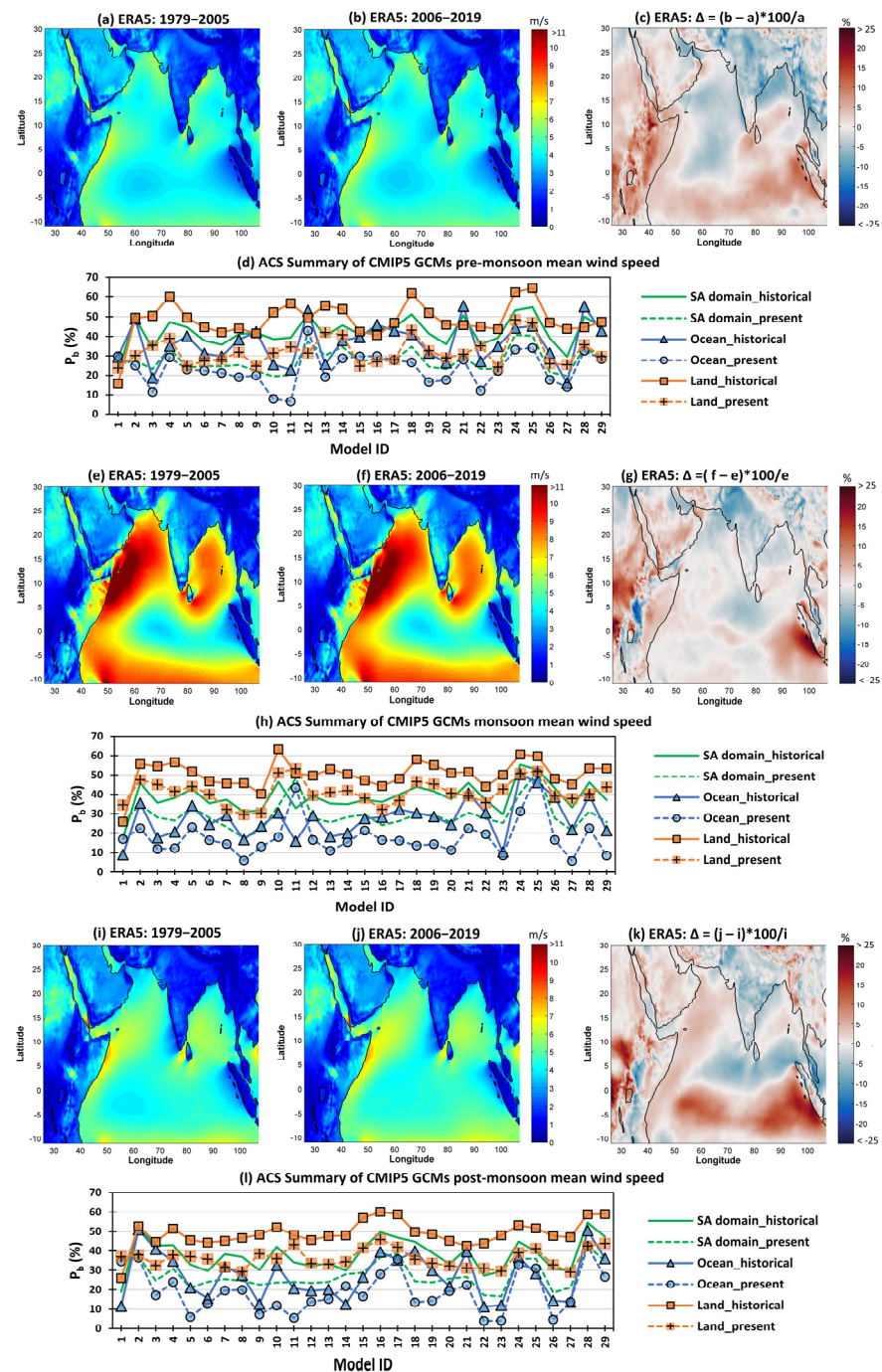


Figure 5. Pre-monsoon (February–May) mean wind speed spatial maps of ERA5 for the (a) historical (1979–2005) and (b) present time slice (2006–2019). (c) Percentage change of present time slice pre-monsoon mean wind speed relative to historical time slice pre-monsoon mean wind speed (Δ , %). (d) As in Figure 2, but summarizes the climate model’s skill in simulating pre-monsoon mean wind speed; percentage of statistically significant bias (P_b , %) on y-axis and Model ID on x-axis. (e–h) As in (a–d), but for monsoon season (June–September). (i–l) As in (a–d), but for post-monsoon season (October–January).

- Pre-monsoon season (February–May)

The observed mean WS from ERA5 is higher along coastal regions of eastern Africa, the eastern and northwestern parts of India, and the Gulf of Mannar, as shown in Figure 5a,b. The pre-monsoon mean WS climate in the present time slice strengthens over southern IO, the African continent, most regions of the Arabian Peninsula, and the southern part of India and Sumatra, and it weakens over AS, the northern part of BoB, and India (refer to Figure 5c). Models 11, 3, 27, and 10 have the lowest P_b value over ocean, and over land model 1 performed well (Figure 5d). Interestingly the models (e.g., model 11, model 1) with higher skill over ocean have lower skill over land, and vice versa. Only model 27 performed well reasonably over ocean and land. Models 24 and 25 consistently show higher P_b over ocean and land in both time slices. The MME_CMIP5 shows moderate performance and the P_b is almost equal over ocean and land.

- Monsoon season (June–September)

The reference ERA5 monsoon mean WS map is shown in Figure 5e,f. The ERA5 accurately captures the most well-known tropical low-level jet known as Somali Jet (Findlater Jet). This jet is an intense cross-equatorial flow that comes from the Southern IO to the central AS and later splits into two branches; one touches the west coast of the Indian subcontinent and another weak branch enters into BoB during the monsoon. The monsoon mean WS is maximum (>10 m/s) near the Somali coast, the northern part of Madagascar, and the southwestern part of AS, and no significant percentage change is observed at the aforementioned locations in the present time slice. The present time slice monsoon mean WS is less ($<$ average percentage change, -2.6%) than the historical time slice monsoon mean WS over the north western region and northeast states of India, along the Great Rift Valley of Africa, the northern tip of Nile River, Persian Gulf, South of AS, and the southwestern region of Sri Lanka. Strengthening ($>10\%$) of weaker monsoon mean WS (<3 m/s) is observed near the Congo River basin of Africa and the western side of Sumatra (Figure 5g). Over the SA domain, models 1 and 8 show higher skill in historical and present time slices, respectively (Figure 5h). Model 23 performed well over ocean but it shows moderate performance over land. Again, models 24 and 25 show poor performance in reproducing the monsoon mean wind climate, whereas MME_CMIP5 shows moderate skill.

- Post-Monsoon season (October–January)

The post-monsoon wind climate pattern is similar to pre-monsoon over IO with a higher mean WS (refer to Figure 5i). The mean WS is higher at central AS and BoB in addition to regions identified in pre-monsoon analysis, and the percentage change is higher in post-monsoon season. In all seasonal scales, the mean WS is increased in the present time slice along the coastal region of Kenya and Somalia and the western part of Sumatra, and decreased in the present time slice over the north western BoB along the Indian coast. Model 1 has higher skill over land and ocean in the historical time slice but it shows below moderate performance in the present time slice (refer to Figure 5l). Overall, models 23 and 22 consistently performed better in both time slices. Model 28 shows poor skill with higher P_b value in both times slices.

MME_CMIP5 shows relatively poor performance in representing post-monsoon WS relative to other seasons. Model 11 reproduces the mean WS climate well in pre-monsoon and post-monsoon, but it is very poor at reproducing monsoon wind climate over ocean, and it performs poorly over land in all three seasons. Likewise, Model 23 performed well in monsoon and post-monsoon, but it shows moderate skill in pre-monsoon. Therefore, the model that performs well in one particular season does not necessarily perform well in another season. However, model 27 consistently performed near to highest skill model in all three seasons over ocean. Over land, only model 1 shows the highest skill in all three seasons. In all seasons, over ocean models 28, 25, 24, 2, and 21, and over land models 25 and 24 show very poor performance. As a result, these models are strongly not recommended for inter-seasonal variation studies.

3.1.5. Seasonal Mean Wind Speed Trend

The presence of a monotonic trend was identified through the Mann–Kendall (MK) test, and trend magnitude was computed by the Theil–Sen slope. Because the sample size ‘n’ is greater than eight, the MK test statistic can be approximated as normally distributed [61]. The standardized MK test statistic Z and p-value are computed at each grid cell of the domain, and the null hypothesis is rejected if the p-value is less than the assumed significance level of 0.1. The grid cells where the trend is statistically significant ($p < 0.1$) are marked with stippling.

- Pre-monsoon seasonal trend

A significant increasing trend is observed over most parts of IO in the historical time slice, whereas a decreasing trend is observed in the present time slice. This change in trend is not captured well by most of the models (refer to Figure 6a–c). Not even a single model performed well over ocean and land in both study time slices, whereas only MME_CMIP5 shows moderate skill consistently. Over the ocean, models 12 and 9 performed well, and over land all models show similar skill and models 2, 3, 14, and 27 performed relatively well. Models 25, 11, 24, and 23 show poor skill over both ocean and land.

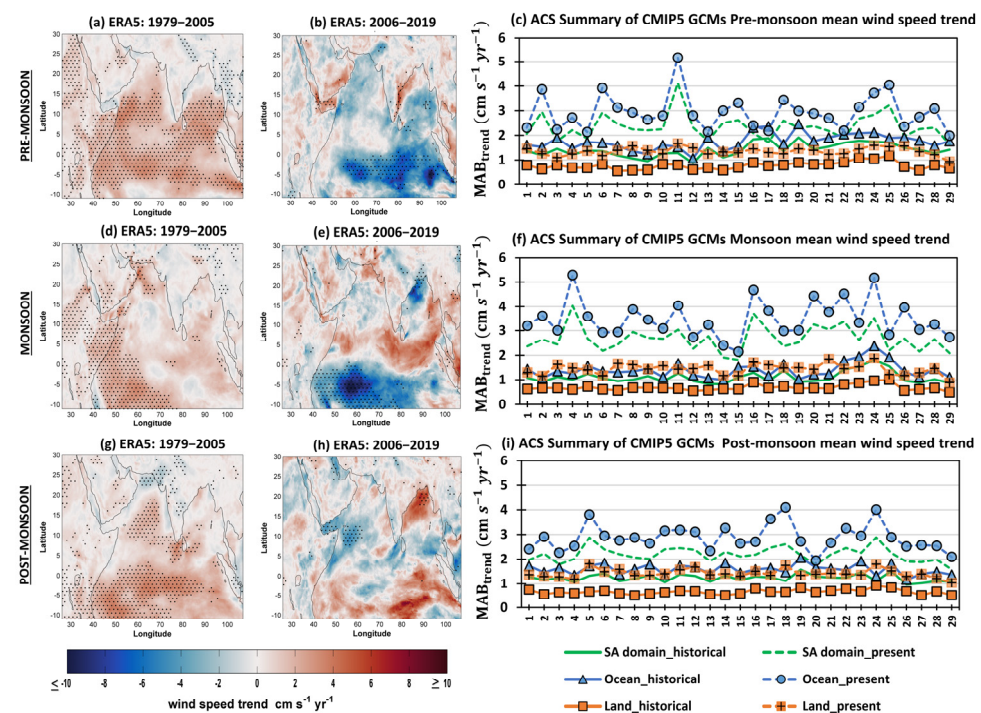


Figure 6. Pre-monsoon (February–May) mean wind speed trend spatial maps of ERA5 for the (a) historical (1979–2005) and (b) present time slice (2006–2019). (c) As in Figure 2, but summarizes the climate model’s skill in simulating pre-monsoon mean wind speed trend; mean absolute bias (MAB, cm/s/yr) on y-axis and Model ID on x-axis. (d–f) As in (a–c), but for monsoon season (June–September). (g–i) As in (a–c), but for post-monsoon season (October–January).

- Monsoon seasonal trend

We know that the monsoon season is dominated with cross equatorial winds, known as Somali Jet. A statistically significant increasing trend is observed along this jet, as shown in Figure 6d. In the present time slice, the weakening of wind field is observed along most regions of Somali jet, and it is higher over most regions of AS and BoB (refer to Figure 6d–f), which indicates the weakening of south-west monsoon. Model 14 and MME_CMIP5 performed well over the ocean in both time slices. Model 24 shows very poor skill over ocean and land in both time slices. The MME_CMIP5 shows the highest skill over land in both time slices.

- Post-monsoon seasonal trend

The statistically significant increasing trend is observed in the historical time slice of post-monsoon season over the south of equatorial region, the southern tip of India, and central AS. In contrast, a decreasing trend is observed over the north of AS and along the central west coast of India (Figure 6g). In the present time slice of the post-monsoon season, a statistically significant increasing trend is observed over the north of BoB, and a decreasing trend is seen over the coastal region of Somalia (Figure 6h). Again, MME performed well over ocean and land in both time slices. Model 14, which performed well at capturing the monsoon mean WS trend, shows poor skill in capturing the post-monsoon WS trend. Model 5 shows very poor skill over ocean and land in both time slices.

The MME_CMIP5 captures the trend magnitude well over three seasons relative to individual models. Most of the models' performance are relatively similar over land in both time slices. In the present time slice over the ocean, higher variability in models' skill is observed, and it is higher in pre-monsoon and monsoon seasons. The decreasing trend over the south of the equatorial region and central AS is observed in all seasons except in post-monsoon. If the observed trend continues in the future, then the mean wind climate will weaken over most parts of IO. Along the east coast of India, the increasing trend is observed in the present time slice in pre-monsoon and post-monsoon, which indicates the strengthening of mean WS climate during north-east monsoon.

3.1.6. Annual Mean Wind Speed

The annual mean WS map of the historical and present time slice is shown in Figure 7a,b. The annual mean WS is higher (> 8 m/sec) off the northeast coast of Africa, southeast and northwest part of Sri Lanka, and north of Madagascar. In the present time slice, a slight increase in annual mean WS climate is observed over most regions of Africa, south of the equator, and in the western Sumatra region. Over the Indian continent, a slight decrease in mean WS is observed in the present time slice (Figure 7c). The ERA5 annual mean wind speed pattern (Figure 7a,b) is similar to the monsoon mean wind speed pattern (Figure 6e,f) with less intensity; thus, monsoon is the dominant pattern over NIO. Most of the bias-corrected CMIP5 GCMs show less P_b in representing annual mean WS climate and more in seasonal mean. The observed mean of all models' P_b (%) over ocean/land is 5.03/19.11, 29.91/40.19, 22.69/45.76, and 23.15/42.56 in representing annual, pre-monsoon, monsoon, and post-monsoon mean WS, respectively. Most of the models perform similarly on the IO, whereas a few models (models 9,10, and 28) have a higher percentage of statistically significant bias on land. The 27-year annual mean is same as the mean of all daily WS due to bias correction with the quantile mapping technique. This technique ensures that all the statistical properties of the model match well with reference data over the considered time slice. However, the statistical properties of models and reference dataset might not match well over the intermediate time slice, which leads to higher bias over the seasonal scale. Thus, the model's skill on the seasonal scale is evaluated considering the weighting factor as one, and zero for the annual mean WS climate assessment.

3.1.7. Annual Mean Wind Speed Trend

Statistically significant increasing annual mean WS is observed over most parts of IO in the historical time slice, and a decreasing trend is observed in the present time slice (Figure 8a,b). In both time slices, the northern part of BoB has an increasing annual mean WS trend. A statistically significant increasing trend was observed in most regions of the South African continent in a historical time slice. The decreasing trend of 1–2 cm/s/year is observed along the central east and west coast of India, and the same was reported by Shanas and Sanil Kumar [39]. Most of the models show similar skill in reproducing the observed annual mean WS trend, whereas model 11 shows poor skill with higher MAB over ocean (Figure 8c). The annual and seasonal mean WS trend patterns show an increasing trend over IO in the historical time slice and decreasing pattern over most parts of IO in

the present time slice. This change in pattern is not captured well by most of the GCMs, which result in higher MAB in capturing the present time slice mean WS trend.

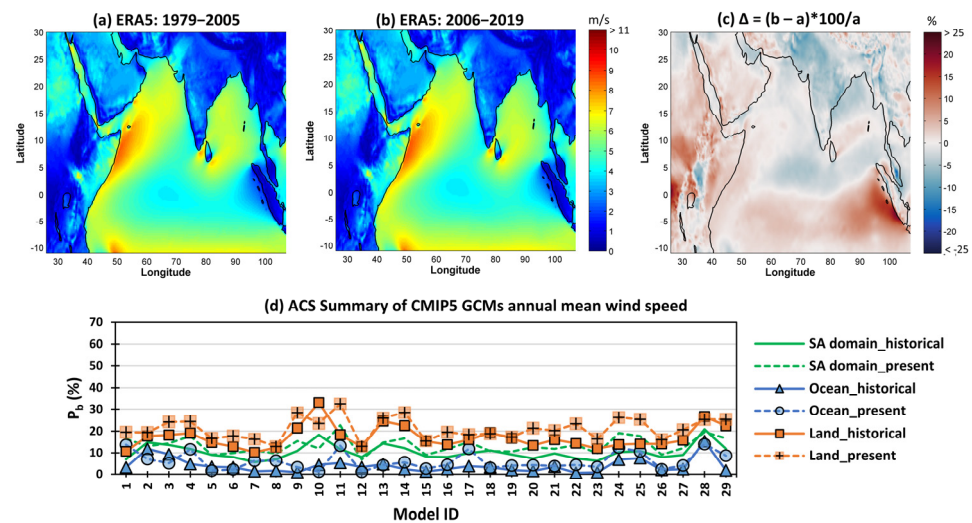


Figure 7. As in Figure 5, but for annual mean wind speed.

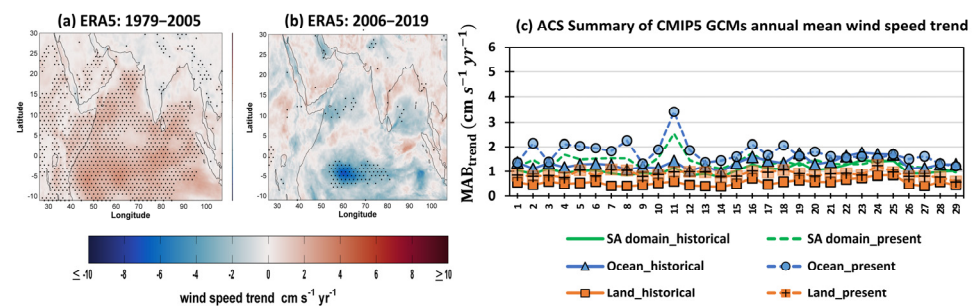


Figure 8. As in Figure 6, but for the annual mean wind speed trend.

3.2. Best Performing Models

The performance of all GCMs in simulating historical and present time slice WS over the SA domain are ranked based on TRS. A summary of estimated TRS over ocean and land is shown in Figures 9 and 10. Based on estimated TRS, the models are divided into the optimum number of groups using k-mean clustering with silhouette score criterion.

Over the ocean, the CMIP5 GCMs are divided into twelve groups with an average silhouette score of 0.8968, and model 27 shows very good skill in both time slices, followed by group 2 models (10 and 13) (refer to Figure 9a). The two-sample t-test is used to test whether model 27 is statistically significantly different from group 2 (model 10 and 13). The result indicates that there is no statistically significant difference between groups 1 and 2 with a p-value of 0.0737. Because the ensemble mean of all models' (MME_CMIP5) skill score is closer to the top two group models, the skill of ensemble mean of group 1 and 2 is evaluated, and greater improvement is observed in all climate variable scales, with the exception of capturing frequency distribution of daily mean WS and EOF1 variance (refer to Figure 9b radar plot). Therefore, the wind climate projections from MME_3_(27, 10, and 13) are recommended for future wave climate impact studies and offshore wind analysis, whereas the individual models of MME_3_(27, 10, and 13) can be used with caution. The sensitivity of model rank with chosen assessment criteria statistic is explored by comparing the rank awarded to a model without considering individual ACS as one scenario. The rankings of the best (models 30 and 27) and worst (models 24 and 25) performing models are found to be the least sensitive to the chosen ACS (Figure S1). Models with TRS close to each other are found to be sensitive to the chosen assessment

criteria. However, considering all ACS (the thick black line) reduces the uncertainty of rank (Figure S1).

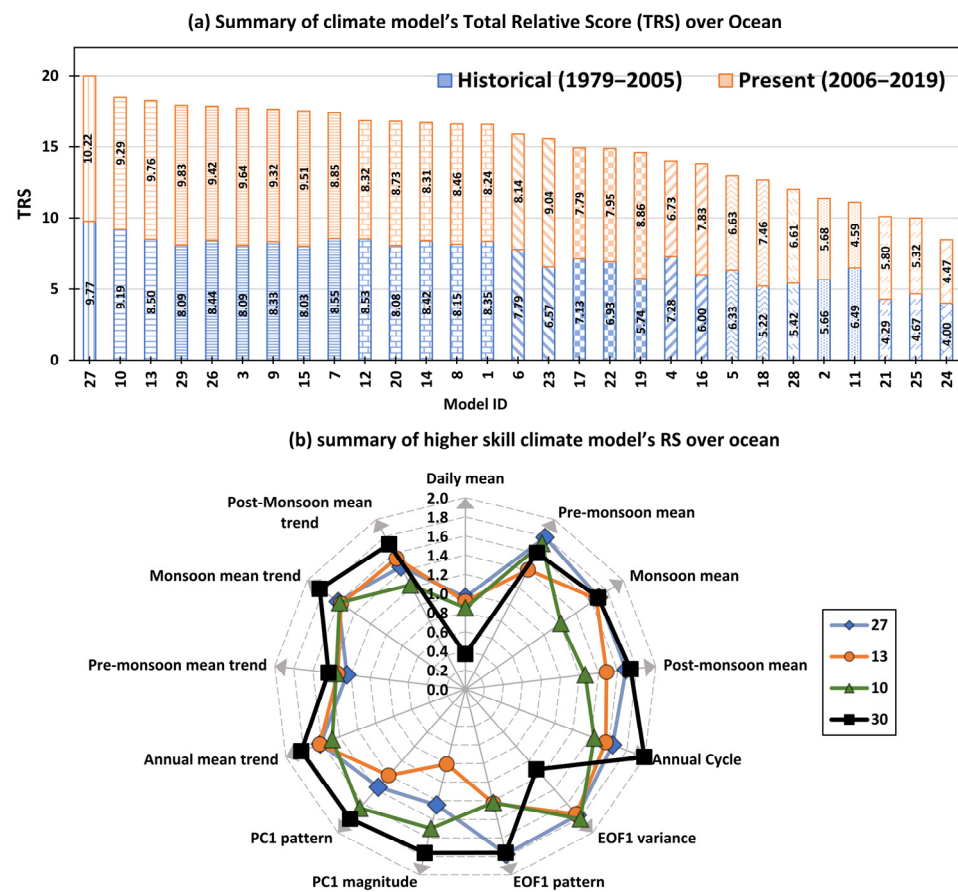


Figure 9. (a) CMIP5 GCM's total relative score (TRS) for historical and present time slice over ocean areas of the South Asian domain. (b) Relative score (RS) of best performing GCMs over different climate variable scales; here RS is the summation of RS obtained in both study time slices in Figure 6, but for annual mean wind speed trend.

Over land, the CMIP5 GCMs are divided into seventeen groups with an average silhouette score of 0.9624; refer to Figure 10a. Not even a single model consistently performed well in all climate variable scales. Models 1, 27, and 15 show relatively better skill in some of the climate variable scales. Model 1 shows better performance than 27 and 15 in reproducing seasonal mean WS, whereas the seasonal and annual mean WS trend is better captured by models 27 and 15 than by model 1 (refer to Figure 10b). The two-sample t-test is used to test whether models 1 and 27 are statistically significantly different from group 3 (models 15 and 29). It is found that there is no statistically significant difference between model 27 and group 3 with a p-value of 0.1049, so model 27 can be added to group 3. A statistically significant difference at a p-value of 0.042 is observed between model 1 and new group 3 (27, 15, and 29). As the p-value is close to 0.05 (assumed significant level) and to get the added advantage of these models, the ensemble mean of all these three models' (with Model ID 31) skill is also evaluated. The results are not as expected in reproducing seasonal mean WS, but better improvement is observed in capturing annual and seasonal mean WS trends.

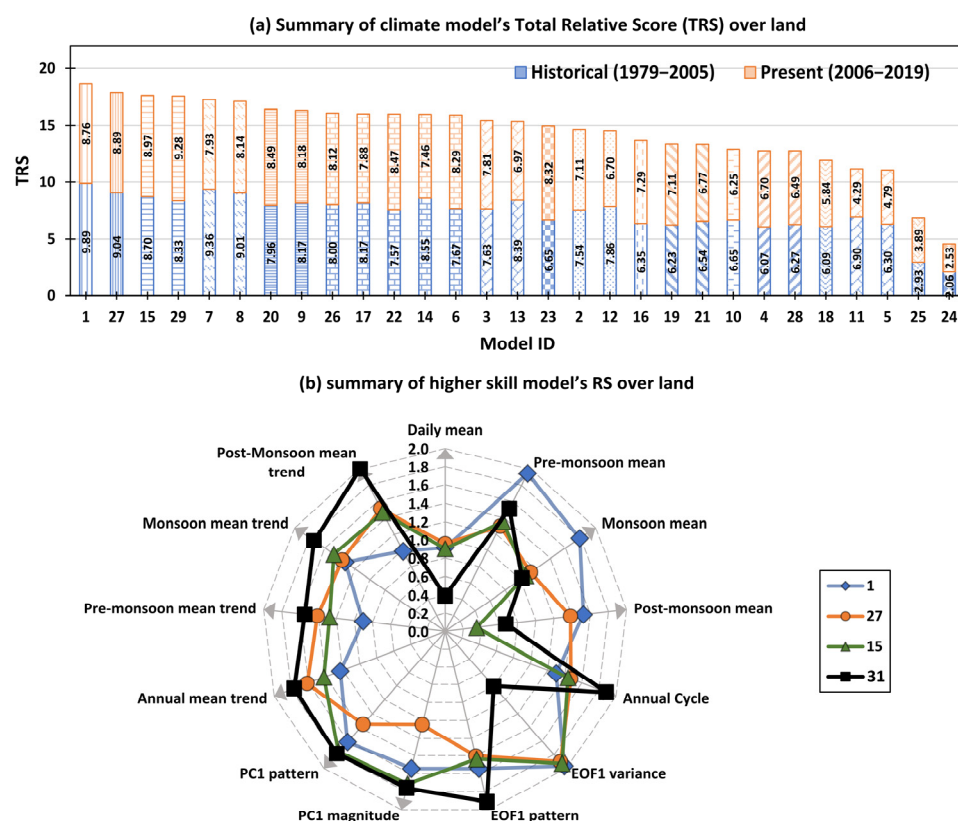


Figure 10. As in Figure 9, but the summary of climate model's skill over land of the South Asian domain.

Only model 27 (MPI-ESM-MR) shows good skill over ocean and land in both time slices. Models 24 (MIROC-ESM) and 25 (MIROC-ESM-CHEM) show the lowest skill over both ocean and land, and these models are strongly not recommended to be used in climate impact studies. The individual climate models are either overestimating or underestimating the wind climate assessment criteria statistic, so the skill of MME_CMIP5 is assessed because it contains information from all the individual models. In this study, the skill of MME_CMIP5 is moderate even though it contains information from all models. This emphasizes that the ensemble of all models need not be always considered as a reliable one. All these above results strongly highlight the importance of careful examination of CMIP5 models before using them for wind potential and risk assessment applications.

We examined the skill of top-performing GCMs with and without bias correction to see how bias correction affected the model's skill. In comparison to GCMs with bias adjustment, the best performing GCMs without bias correction have the lowest skill (Figures S2a and S3a). The ensemble model constructed from top-performing models has a greater TRS than individual top-performing models, regardless of whether bias correction is used (Figures S2b and S3b). In comparison to GCMs without bias correction, bias-corrected GCMs demonstrate a significant increase in skill across all climatic variable scales (except in reproducing the annual and seasonal mean WS trend) (Figures S2c and S3c). The bias correction of GCMs results in a 40% increase in TRS on average. Thus, bias correction has a greater effect on reducing the model's systematic bias, and the rank of a model is less susceptible to bias correction.

The climate models have very low atmospheric spatial resolution relative to ERA5. In general, there are two approaches to deal with low spatial resolution climate models: either regrid the climate model data to the spatial resolution of the reference model or regrid the reference model to the spatial resolution of the climate model dataset, and assess the skill of the climate models. To check the reliability of both approaches, let us consider the top three low-resolution climate models (BNU-ESM, CanCM4, and CanESM2) and estimate the ACS value from both approaches (refer to Section 2.2 for more details on methodology).

Figure S4 shows a summary of the estimated ACS. In all climate variable scales, there is not much significant difference between both approaches observed (Figure S4). In most of the climate variable scales, the current study approach shows slightly lower ACS. Further, it is important to rank climate models as per their performance. In general, we use a suitable statistic (in our case ACS is a statistic) to summarize the skill of a climate model. It is important that the sample size used to estimate the statistic should be same for each model for the intercomparison of models. If we regrid the reference dataset to the climate model grid resolution, the sample size used to compute the ACS will differ due to the different spatial resolution (i.e., different number of grid points) of the climate models. Therefore, utilizing the ACS obtained from the various sample sizes to estimate the relative score and ranking of climate models is inappropriate and will lead to a wrong inference. The current study approach can be used for evaluating the relative skill of low-resolution climate models in representing wind speed climate over SA domain. However, this may vary if different climate variables are considered.

3.3. Intercomparison of CMIP5 GCMs

As CMIP moves from one phase to another phase, it develops complex and sophisticated earth system models (ESMs) by including more processes and models to fill the scientific gaps identified in the earlier phase [62]. However, the added advantage of including complex processes (like carbon-cycle dynamics) in reducing the bias in WS is not clear yet. In general, as we move from atmosphere only GCMs (AGCMs), to coupled atmosphere-ocean GCMs (AOGCMs) to fully coupled ESMs, the processes are better represented with a possible reduction in systematic errors. However, in the current study, there are thirteen ESMs, two ChemESMs, and thirteen AOGCMs; and it is expected that ESMs should perform well compared to AOGCMs as they consider a higher number of processes and model components. In the current study, top-performing GCM in representing the WS over ocean and land are ESM (MPI-ESM-MR) and AOGCM (ACCESS1.0), respectively. At the same time, Model 24 (MIROC-ESM) is the worst-performing model, which is an ESM. This highlights the need for understanding the contribution of different dynamical components used in the particular model. To answer whether increasing the horizontal or vertical resolution improves the model's skill, and do the models from the same institute show similar skills or not, we carried out the inter-model comparison of models' skill based on estimated TRS.

Over the ocean and land, MPI-ESM-MR TRS is 11.96% and 11.17% greater than MPI-ESM-LR, respectively. This can be attributed to an increase in vertical levels (from 47 to 95) of the atmosphere component (ECHAM6) and a finer horizontal grid resolution of the ocean component (MPIOM) from 1.5° to 0.4° in MPI-ESM-MR compared to MPI-ESM-LR. Müller et al. [63] observed that increasing the atmospheric resolution of MPI-ESM1.2-HR can reduce the biases of the upper-level zonal wind and atmospheric jet stream position in the northern extratropics. MIROC5 and MIROC4h are AOGCMs with similar model configurations, whereas MIROC4h has higher atmospheric grid resolution (4 times). When we compared the skill of both models, the MIROC4h model has 7.17% higher TRS over land, which highlights the benefit of using the higher atmospheric grid resolution models over land. CMCC-CM and CMCC-CMS are AOGCMs with similar model configurations, where CMCC-CM has a higher atmospheric horizontal resolution (2.5 times) and CMCC-CMS has higher stratospheric vertical resolution (3 times). TRS of CMCC-CM is 4.69% higher over ocean and 0.86% higher over land than the CMCC-CMS. These results signify that atmospheric horizontal and vertical resolution has a moderate impact on near-surface WS simulation the over SA domain. The MPI-ESM-MR is the best performing model over the SA domain, even though it is not a high spatial resolution model. Moreover, MPI-ESM-MR has TRS 34.31% and 11.76% higher than the high spatial resolution model (MIROC4h, $0.56^\circ \times 0.56^\circ$) over ocean and land, respectively. Even though the CanESM2 is the low spatial resolution ($2.8125^\circ \times 2.8125^\circ$) model, CanESM2 has TRS 6.52% higher than MIROC4h over the ocean, and both have similar skill over land. Despite having a similar

spatial resolution, the skill of CanESM2 is 22.91% and 43.84% higher than CanCM4 over ocean and land, respectively. Therefore, the model with high or low atmospheric spatial resolution does not necessarily exhibit the best or worst skill, respectively, whereas the dynamic components in the model configuration play a major role.

ACCESS1.0 and ACCESS1.3 have similar ocean components (NOAA/GFDL MOM4p1 model), sea-ice components (CICE), and atmospheric grid resolution, but they differ from each other in atmospheric physics and land surface components. ACCESS1.0 uses UK Met Office HadGEM2 (r1.1) atmospheric physics and MOSES2 land surface models, whereas ACCESS1.3 uses UK Met Office Global Atmosphere 1.0 atmospheric physics and CABLE land surface models [64,65]. ACCESS1.0 has TRS 46.12% and 27.33% higher than ACCESS1.3 over ocean and land, respectively. Even though both models have the same ocean component, there is a significantly higher difference in models' skill over ocean compared to land. This highlights the contribution of atmospheric and land components over the ocean component in simulating WS. Zha et al. [66] also found that ACCESS1.0 performs better than ACCESS1.3 in capturing interannual variability of WS over eastern China.

CanESM2 differs from CanCM4 by adding vegetation (CTEM1) and carbon cycle (CMOC1.2) components [67], and these added components could have increased the skill of CanESM2 by 22.91% over the ocean and 43.84% over land in simulating WS over SA domain. However, further detailed investigation is required to quantify the contribution of each component.

HadGEM2-AO is an AOGCM, which has atmosphere (HadGAM), ocean (HadGOM2), and sea-ice components. The addition of terrestrial carbon cycle (TRIFFID) and ocean biogeochemistry (diat-HadOCC) to HadGEM2-AO constitutes the HadGEM2-CC model [68]. The ecosystem components (TRIFFID and diat-HadOCC) of HadGEM2-CC, which models the exchange of carbon dioxide between the atmosphere, terrestrial biosphere, and oceanic biosphere, might have reduced the HadGEM2-CC skill by 26.82% over ocean and 29.52% over land relative to HadGEM2-AO, respectively. Similarly, the skill of MIROC-ESM in representing WS over SA domain has been reduced (75.77% over ocean and 249.53% over land) due to additional ecosystem components (SEIB-DGVM and NPZD) and lower (five times) atmospheric grid resolution of MIROC-ESM compared to MIROC4h. The higher reduction in MIROC family GCMs' skill relative to the HadGEM2 family GCMs can be attributed to a higher reduction in atmospheric resolution. In a recent study, Morim et al. [12] highlighted that we can expect no major change in CMIP6 climate models (with carbon-cycle component) wind simulation at decadal time slices.

The HadGEM2-ES has 7.9% higher skill over the ocean and 17.68% higher skill over the land compared to HadGEM2-CC, where HadGEM2-ES has an atmospheric chemistry component (UKCA tropospheric chemistry scheme) in addition to the HadGEM2-CC model components. Similarly, due to the additional atmospheric chemistry component (CHASER 4.1) of MIROC-ESM-CHEM relative to MIROC-ESM has improved the skill of the former model in representing the WS over the SA domain (17.97% over ocean and 48.65% over land). Watanabe et al. [69] show MIROC-ESM-CHEM has good skill in reproducing earth system climate in the historical period (1850–2005) relative to MIROC-ESM.

Even though most sophisticated ChemESMs' (HadGEM2-ES, MIROC-ESM-CHEM) skill is higher than their respective ESMs (HadGEM2-CC, MIROC-ESM), the simple AOGCMs (HadGEM2-AO, MIROC4h) have higher skill compared to ChemESMs (HadGEM2-ES, MIROC-ESM-CHEM) in representing WS over the SA domain. HadGEM2-AO has 17.54% and 10.06% higher TRS than HadGEM2-ES over ocean and land, respectively. MIROC4h has 48.99% and 135.14% higher TRS than MIROC-ESM-CHEM over ocean and land, respectively. The extra complexity in ESMs can lead to increased uncertainty in their prediction, and it is important to observe that considering all dynamical components is not necessary for all purposes [70].

GFDL-ESM2G and GFDL-ESM2M are ESMs with similar model configuration and resolution, but they differ in physical ocean component; GFDL-ESM2M uses Modular Ocean Model version 4p1 (MOM4p1) with vertical pressure layers, whereas GFDL-ESM2G uses

Generalized Ocean Layer Dynamics (GOLD) with a bulk mixed layer and interior isopycnal layers [71]. Over the ocean and land, the GFDL-ESM2G and GFDL-ESM2M have 9.18% and 4.28% higher TRS than GFDL-ESM2M and GFDL-ESM2G, respectively. GFDL-CM3 and GFDL-ESM2M show similar skills (with a difference of 0.74% in TRS) over the ocean with similar ocean components, which is also observed by Dunne et al. [72]. IPSL-CM5A-LR and IPSL-CM5A-MR models have the same model configurations [73], whereas the former model has a low atmospheric resolution (~1.5 times), which could be the reason behind the decrease in its TRS over the ocean and land by 15.13% and 23.44%, respectively, compared to IPSL-CM5A-MR. IPSL-CM5A-LR has another version named IPSL-CM5B-LR, which has all components and parameters similar to IPSL-CM5A-LR except for the atmosphere component [74]. However, the change in the skill of IPSL family GCMs in simulating WS over the SA domain due to a difference in atmosphere component (6.77% over ocean; 0.3% over land) compared to the changes due to difference in atmospheric resolution. A recent study by Morim et al. [12] found that improving the atmospheric component results in a greater reduction in wind bias compared to land surface component, ocean component, sea-ice component, land carbon, and ocean carbon component. Morim et al. [12] show inter-model uncertainty is higher (~2–4 times) than GCM internal variability. The performance of CMIP6 models relative to CMIP5 in representing the near-surface wind climate over the SA domain is largely unknown, and it worth investigating the differences in near-surface wind projections, if significant. Krishnan and Bhaskaran [22] performed the inter-comparison of CMIP5 and CMIP6 models with reference to ERA-Interim and Scatterometer datasets over the BoB and observed that a higher number of CMIP6 models captured the monthly mean WS pattern with correlation range of 0.8–0.9 and with root mean square error (RMSE) of 1–1.5 m/s. However, the CNRM-CM5 CMIP5 GCM captured the magnitude, variance, and pattern of monthly mean WS near to reference datasets compared to all CMIP6 individual models. The Nash–Sutcliffe efficiency score for MME of best-performing models from CMIP6 is 10.94% and 16.13% higher than MME of best-performing models from CMIP5 compared to ERA-Interim and Scatterometer datasets, respectively. A single model always has its limitation in the application, which leads to the development of a new state of models by refining the processes in the model configuration that are essential to answer certain scientific questions and to address different applications [68]. However, the quantification of the significant improvement from next-generation GCMs in representing historical and present wind climate is essential before using them in impact studies. Investigating the mechanisms responsible for inter and intra model skill differences is beyond the scope of this analysis.

3.4. Future Wind Speed Projections

The percentage change in the future mean WS relative to historical mean WS is examined in annual and seasonal scales over the ocean (Figures 11 and 12) and land (Figures 13 and 14) using WS projections from best-performing climate models (MME-3_(27,10, and 13) for ocean and ACCESS1.0 for land parts of the SA domain).

In the near-term, minor (average 1.5%) strengthening of annual mean WS is observed over most parts of AS, BoB, and the southern equatorial region, and it weakens over most parts of IO in mid-term for in both scenarios (Figure 11). This weakening of annual mean WS is enhanced further by the end of 21st century for the RCP8.5 scenario (Figure 11j–l) over the SA domain. The weakening of annual mean WS is higher over the central northern equatorial region and central AS compared to other regions of the SA domain, which is corroborated by Mohan and Bhaskaran [21].

Strengthening of pre-monsoon mean wind speed is observed over the AS, northern BoB, Gulf of Thailand, Strait of Malacca, and central southern equatorial region (lesser strengthening), and weakening is observed over the Persian Gulf, Gulf of Oman, south-east BoB, and western equatorial IO in the near-term (Figure 12i(a,g)). Irrespective of the RCP scenario, the weakening of pre-monsoon WS is observed in future-term relative to near-term over 88% of the SA domain (central AS, BoB, and southern equatorial region), and the

magnitude of change in percentage change is higher for RCP8.5 scenario (Figure 12I(f,l)). In the future-term, the weakening of pre-monsoon mean WS relative to historical mean pre-monsoon WS is observed over 54.28% and 65.07% of the IO for the RCP4.5 and RCP8.5 scenarios, respectively (Figure 12I(c,i)).

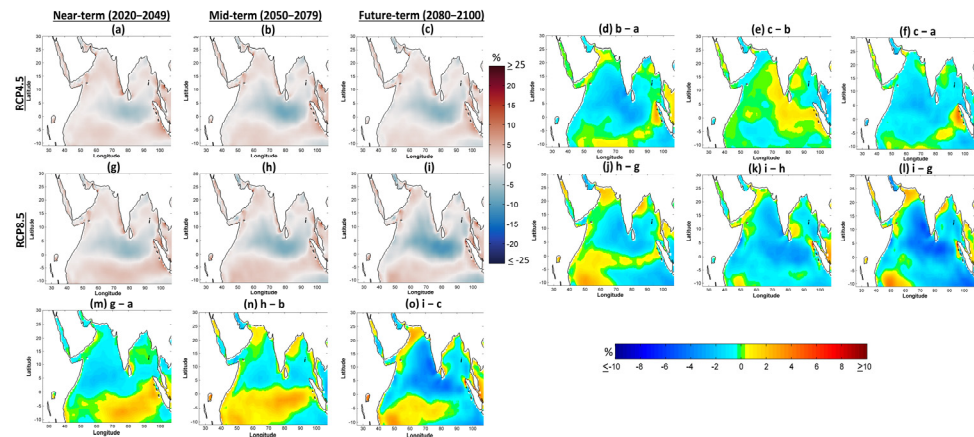


Figure 11. (a) For the RCP4.5 scenario, the percentage change in near-term annual mean wind speed estimated from MME-3_(27,10, and 13) model projections relative to the ERA5 historical time slice (1979–2005) over the ocean. (b) As in (a), but for the mid-term RCP4.5 scenario. (c) As in (a), but for the future-term RCP4.5 scenario. The difference in percentage change in annual mean wind speed from (d) near-term to mid-term, (e) mid-term to future-term, and (f) near-term to future-term, for the RCP4.5 scenario. (g–i) As in (a–f), but for the RCP8.5 scenario. (m) The difference in percentage change in near-term annual mean wind speed from the RCP4.5 to the RCP8.5 scenario. (n) As in (m), but for the mid-term. (o) As in (m), but for the future-term.

Interestingly, over the near-equatorial region where weaker (<3 m/s) historical monsoon mean WS is observed (Figure 5e), it has strengthened by the end of 21st century, and this strengthening is higher near the west coast of Sumatra ($>15\%$ for RCP4.5 and $>22\%$ for RCP8.5) (Figure 12II(c,i)). Irrespective of the RCP scenario, higher weakening ($<-6\%$ for RCP4.5 and $<-10\%$ for RCP8.5) of monsoon mean wind speed is observed over the south of AS, north of BoB, and north of the equatorial region in the future-term relative to historical term (Figure 12II(c,i)). Enhancement in percentage change of monsoon mean WS is observed from near-term to mid-term in both scenarios (Figure 12II(d,j)), but this enhancement continued from mid-term to future-term only for the RCP8.5 scenario over most parts of the IO (Figure 12II(e,k)).

The strengthening of post-monsoon mean WS is observed along most regions of Somali jet, and weakening over northern AS, along the continental region of BoB, the central equatorial region, and south of Sumatra. The strengthening of post-monsoon mean WS is higher ($>30\%$) along the southwest coast of India (Figure 12III). For the RCP8.5 scenario, the weakening of post-monsoon mean WS is observed over eighty percent of IO (except over the southern tip of India, south of BoB, and Gulf of Thailand, and west of the southern equatorial region of IO) in future term relative to near-term WS (Figure 12III l). Along the waters of the western coast of Sumatra, a decreasing percentage change is observed, which is the opposite of the pattern observed in the present time slice (Figures 5k and 12III). Similarly, an increasing percentage change in pre-monsoon mean WS is observed over AS and BoB in future-terms, but a decreasing percentage change is observed in the present time slice (refer to Figures 5c and 12I). The highest percentage change (121.17% for RCP4.5, 114.52% for RCP8.5) in post-monsoon mean wind speed is observed near the southern tip of India (latitude 8.25° , longitude 77°) in the near-term.

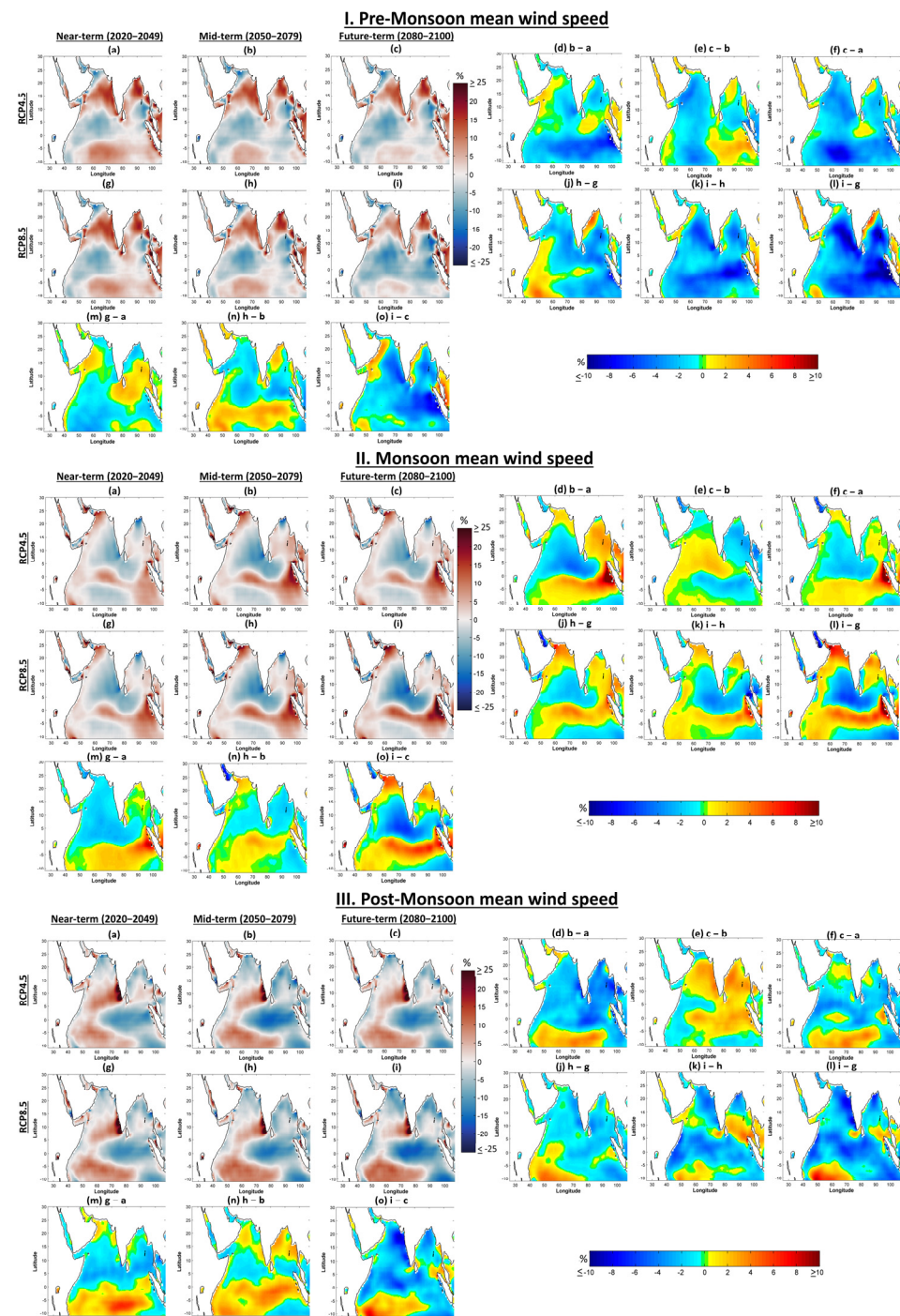


Figure 12. As in Figure 11, but for (I) pre-monsoon (February–May), (II) monsoon (June–September), and (III) post-monsoon (October–January).

The application of RCP4.5 in climate models is to study the response of long-term climate systems to the scenario of stabilizing the anthropogenic components of radiative forcing [75]. The radiative forcing increases by $\sim 46\%$ in the near-term (from 2.57 to 3.75 W/m^2), by $\sim 13\%$ in the mid-term (from 3.76 to 4.25 W/m^2), and by $\sim 1.41\%$ in the future-term (from 4.25 to 4.31) (data extracted from RCP database URL: http://tntcat.iiasa.ac.at/RcpDb/download/R45_bulk.xls; accessed on 10 September 2021). Similar to RCP4.5 radiative forcing change, the WS projections show higher percentage change in the near-term, and lower percentage change from mid-term to future-term. More importantly, for RCP4.5 mostly in all climate variable scales, the percentage change from

mid-term to future-term is opposite of the percentage change observed from near-term to mid-term, which results in stabilization of mean WS without much change from the near-term. This indicates the importance of the stabilization of anthropogenic components of radiative forcing. Unlike RCP4.5 for RCP8.5, whatever the percentage change in the mean WS climate is observed from near term to mid-term continues to future-term. The percentage change from near-term to future-term is higher for RCP8.5 compared to RCP4.5. Overall, the weakening of mean WS near central-northern equatorial region is observed in all climate variable scales. The magnitude of percentage change in mean WS over annual scales is lesser than the seasonal scales.

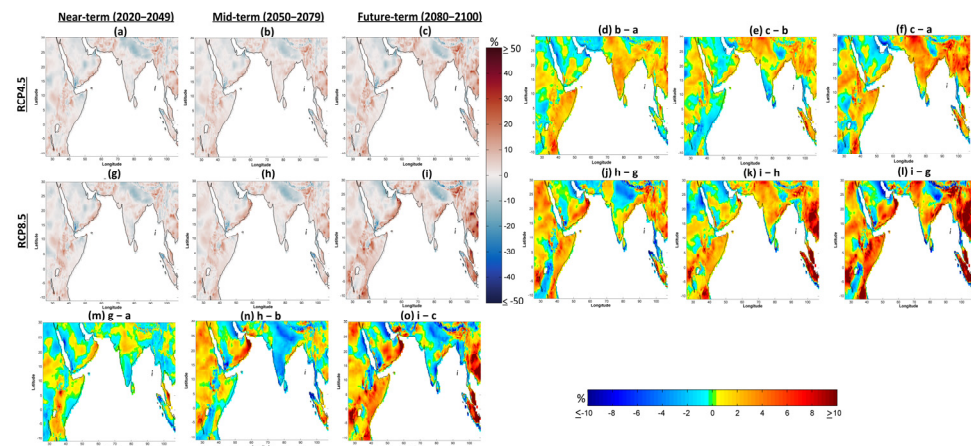


Figure 13. As in Figure 11, but for annual mean wind speed over land region of South Asian domain, and the percentage change is calculated based on projections of ACCESS1.0.

The annual mean WS is observed to strengthen over 64.14% of SA and weaken over 35.86% of SA subcontinent with an average percentage change of 4.78% and -3.33% , respectively, by the future-term for the RCP4.5 scenario (Figure 13a–c). The percentage change pattern is similar for both RCP scenarios, but the magnitude of percentage change is higher for the RCP8.5 scenario (approximately 24.41% increase at the highest percentage change point (latitude 18.75° , longitude 102.75°) than is observed for the RCP8.5 scenario). The strengthening ($>15\%$) of annual mean WS is observed over Thailand, Malaysia, and Sumatra, and weakening ($<-10\%$) of annual mean WS is observed over the coastal region of the Persian Gulf, the northern plain of India, and Himalaya range in the future-term for the RCP8.5 scenario (Figure 13i).

In both RCP scenarios, the strengthening ($>15\%$) of pre-monsoon mean WS is observed over eastern Africa, the south-west coast of India, the north-east coast of India, north of the Himalaya range, and Myanmar, Thailand, Malaysia, and Sumatra in the near term, and this change strongly strengthens (with a maximum increase of 68.05% for RCP8.5 and 23.73% for RCP4.5) in the future-term (Figure 14i). In the future-term, the highest increase in the percentage change relative to historical mean WS is observed north of the Himalaya range (latitude 29.75° , longitude 95°) with 104.6% and 114.28% for the RCP4.5 and RCP8.5 scenarios, respectively.

Over the northwestern part of India, the weakening of future WS is observed in pre and post-monsoon season, whereas strengthening of future WS is observed in monsoon season. Similarly, over Saudi Arabia, weakening of future WS in monsoon season and strengthening in pre and post-monsoon seasons is observed (Figure 14). In both RCP scenarios, the average increase in percentage change of future-term mean WS over land is higher for monsoon season, followed by post-monsoon and pre-monsoon. The 203.69% and 216.65% change in future-term monsoon mean WS relative to historical mean WS is observed at the north of Ethiopia (latitude 14° , longitude 38°) for RCP4.5 and RCP8.5 scenarios, respectively. Unlike over the ocean, the enhancement in percentage change is higher over land relative to the ocean. Significant changes in the 21st century annual

and seasonal mean WS are observed, and it is expected that these changes in WS will have a significant impact on wind-driven processes (like wind waves). This impact can be quantified using the recommended best-performing climate model projections.

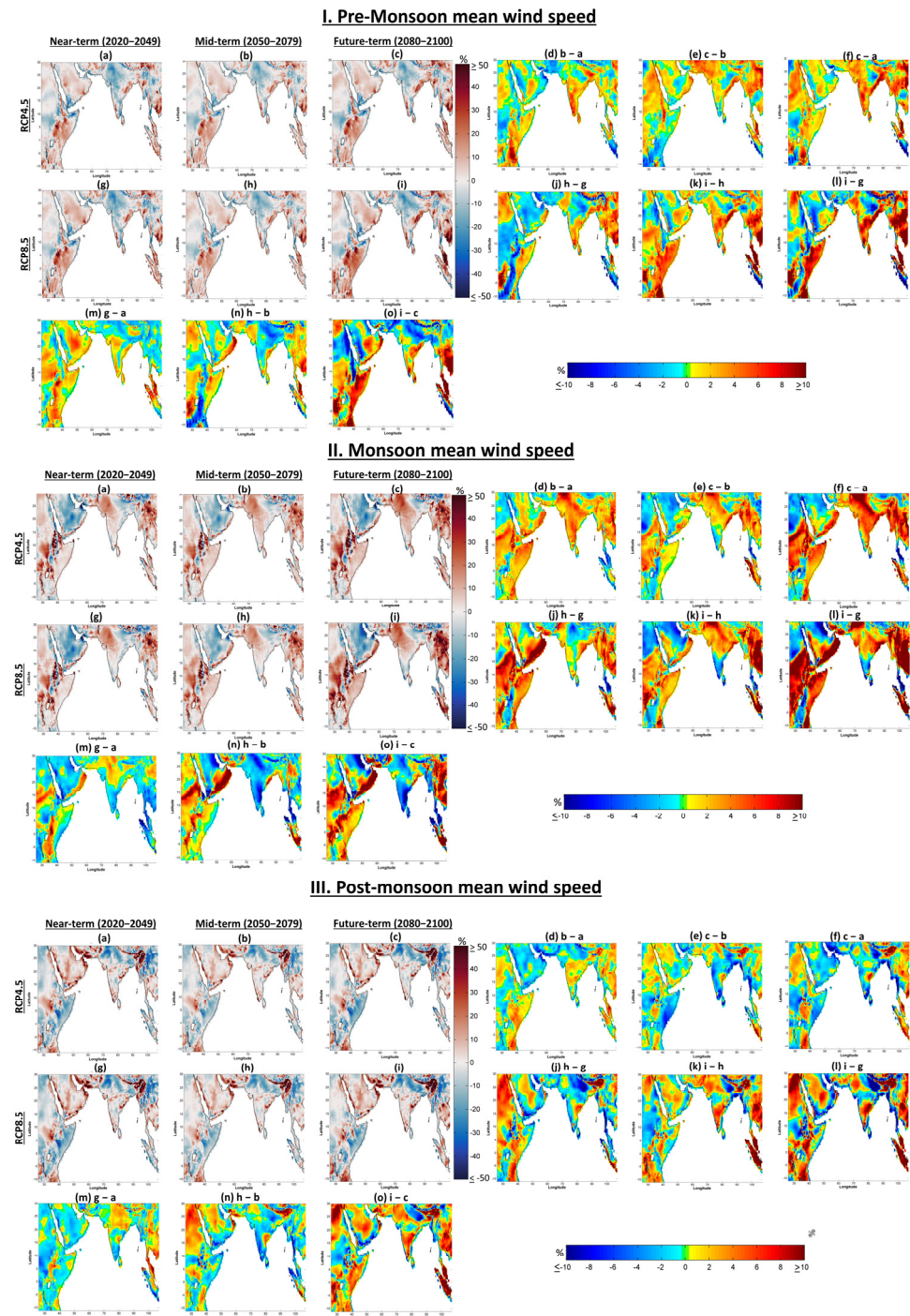


Figure 14. As in Figure 11, but for (I) pre-monsoon (February–May), (II) monsoon (June–September), and (III) post-monsoon (October–January) mean wind speed over land region of South Asian domain, and the percentage change is calculated based on projections of ACCESS1.0.

4. Conclusions

The current study evaluated the performance of twenty-eight available CMIP5 GCMs in representing near-surface wind speed relative to reanalysis ERA5 data over the South Asian (SA) domain. A new relative score-based approach has been used to assess the ability of each GCM to represent frequency density of daily mean wind speed, long-term monthly mean wind speed variation (annual cycle), mean and trend of annual and seasonal wind speed, and spatio-temporal variability of monthly mean wind speed. Upon inspection of a model's skill over diverse climate variable scales, it is observed that judging a model's performance based on its competence on a certain climatic variable scale (e.g., monthly mean or annual mean, etc.) is not advised.

The intercomparison of GCMs from the same family is performed using an estimated total relative score to understand the role of different dynamic components and spatial resolution (horizontal and vertical) in model skill. A significant benefit is observed in using higher resolution models over land compared to the ocean. The intermodal comparison of GCMs having a similar model configuration with the difference in spatial resolution highlight that increasing horizontal and vertical resolution has a moderate impact on near-surface wind speed simulation over the SA domain. However, when we compared the GCMs having the lowest or highest spatial resolution with different model configurations, we observed that the model with the highest or lowest spatial resolution did not necessarily exhibit the best or worst performance, respectively, whereas the dynamic components in the model configuration play the major role. The changes in sea-ice and ocean model components have a lesser effect on wind speed simulation, whereas the atmosphere component (with or without tropospheric chemistry) and land component have significant effects. Although the current study evaluates the performance of all available CMIP5 GCMs, it is expected that further investigation can be carried out to decode the model variability and bias in GCMs.

Overall, the 27-MPI-ESM-MR, 10-CSIRO-Mk3.6.0, and 13-GFDL-ESM2G are the top-performing individual GCMs over the ocean. The ensemble of these three models' (MME-3_(27, 10, and 13)) skill is higher and demonstrates greater improvement at all climate variable scales, except in representing frequency distribution of daily mean wind speed and EOF1 variance. Over the land, 1-ACCESS1.0, 27-MPI-ESM-MR and 15-HadGEM2-AO show higher skills in most of the assessment criteria. In conclusion, the wind climate from MME-3_(27, 10, and 13) is recommended for future wave climate impact studies and offshore wind analysis. Over the land, MME-3_(1, 27, and 15) model wind projections are recommended for mean wind speed trend analysis and 1-ACCESS1.3 for mean wind speed analysis. It is strongly not recommended to use the MIROC-ESM and MIROC-ESM-CHEM models in wind-driven climate change impact studies.

This study also investigated the percentage change in annual and seasonal mean wind speed for the near-term (2020–2049), mid-term (2050–2079), and future-term (2080–2100) relative to historical (1979–2005) time slice from the best-performing models over ocean and land for the RCP4.5 and RCP8.5 scenarios. The future projected changes in near-surface wind speed are found to be significant for RCP4.5, with even greater changes observed for the RCP8.5 scenario because RCP8.5 replicates the scenario of the largest increase in greenhouse gas concentration level by the end of 2100 [76]. In the future-term, strengthening and weakening of mean wind speed is observed over most regions of SA land and ocean, respectively. The magnitude of overall domain average percentage change is higher over land compared to the ocean. The annual mean wind speed percentage change is lesser compared to seasonal scale change. In all climate variable scales, the weakening of wind speed from near-term to future-term is observed over the southern Arabian Sea and central northern equatorial region of the Indian Ocean. Over the land, the strengthening of mean wind speed is observed on the coastal plain of the United Republic of Tanzania, Oman coast, Thailand, and Sumatra, and weakening is observed over the central northern plains of India on both annual and seasonal scales. The mechanisms responsible for changes in

future wind projections can be studied by examining the variability in sea level pressure, sea surface temperature, and surface air temperature.

Supplementary Materials: The following are available online at <https://www.mdpi.com/article/10.3390/atmos13060864/s1>, Figure S1: Sensitivity of climate model's rank with chosen assessment criteria over ocean areas of South Asian domain. Climate model rank obtained by removing a specific assessment criterion are marked with right pointed triangle markers for without evaluating daily mean wind speed, square markers for without evaluating the seasonal mean wind speed, diamond markers for without evaluating the long-term monthly mean wind speed pattern (annual cycle), left pointed triangle markers for without consideration of empirical orthogonal function (EOF) analysis, cross sign markers for without evaluating annual mean wind speed trend, and plus sign markers for without evaluating seasonal mean wind speed trend. The bubble size indicates total how many cases (out of seven) have given a particular rank to a climate model. For example, Model 30 and Model 27 have secured the first rank in all seven cases. The thick black line is the result case obtained by considering all the assessment criteria, and it passes through the largest bubble at most of the ranks. The interchange of a particular rank is observed between the climate models whose total relative score is near to each other, Figure S2: Summary of GCMs skill over ocean areas of the South Asian domain. (a) Total relative score (TRS) of bias-corrected GCMs vs. top-performing GCMs without bias correction. Summary of best performing GCMs with and without bias correction (b) TRS, and (c) relative score over multiple climate variable scales; the model ID with an asterisk (*) represents the GCM without bias correction, Figure S3: As in Figure S2, but represents a summary of GCMs skill over land areas of the South Asian domain, Figure S4. Assessment criterion statistic (ACS) summary of the top three low-resolution climate models (BNU-ESM, CanCM4, and CanESM2) over the entire South Asian domain in representing (a) daily mean wind speed, (b) annual and seasonal mean wind speed, (c) long-term monthly mean (annual cycle), (d) annual and seasonal mean wind speed trend, (e-h) spatio-temporal variability of monthly mean wind speed. The x-axis represents the model acronym and the y-axis represents ACS. The model acronym with an asterisk (*) is the result case where the reference dataset is regridded to the spatial resolution of climate models and applied the suitable statistical metric to assess the skill of the climate model relative to the reference dataset. The model acronym without an asterisk (*) is the result case where the climate model dataset is regridded to the spatial resolution of the reference dataset and applied the suitable statistical metric to assess the skill of the climate model relative to the reference dataset.

Author Contributions: Conceptualization, N.K.G.L. and M.R.B.; data curation, N.K.G.L. and M.R.B.; formal analysis, N.K.G.L. and M.R.B.; methodology, N.K.G.L. and M.R.B.; resources, N.K.G.L. and M.R.B.; software, N.K.G.L. and M.R.B.; supervision, M.R.B.; validation, N.K.G.L. and M.R.B.; visualization, N.K.G.L. and M.R.B.; writing—original draft, N.K.G.L.; writing—review and editing, N.K.G.L. and M.R.B. All authors have read and agreed to the published version of the manuscript.

Funding: This research received no external funding.

Institutional Review Board Statement: Not applicable.

Informed Consent Statement: Not applicable.

Data Availability Statement: The data of CMIP5 GCMs are downloaded from Earth System Grid Federation (ESGF) portal (<https://esgf-node.llnl.gov/search/cmip5/>, accessed on 11 January 2021). The data of ERA5 are downloaded from Copernicus Climate Change Service (C3S) Climate Data Store (<https://cds.climate.copernicus.eu/>, accessed on 21 January 2020).

Acknowledgments: Naresh K. G. Lakku acknowledges support from Prime Minister's Research Fellowship (PMRF). Authors acknowledge the World Climate Research Program's Working Group on Coupled Modelling for making CMIP5 GCM outputs available (listed in Table 1). The authors also acknowledge European Centre for Medium Range Weather Forecasts for providing the ERA5 wind dataset. The authors gratefully acknowledge the critical comments, thoughtful questions, and recommendations from all the anonymous reviewers for improving the quality of the paper.

Conflicts of Interest: The authors declare no conflict of interest.

References

- Nabipour, N.; Mosavi, A.; Hajnal, E.; Nadai, L.; Shamshirband, S.; Chau, K.W. Modeling Climate Change Impact on Wind Power Resources Using Adaptive Neuro-Fuzzy Inference System. *Eng. Appl. Comput. Fluid Mech.* **2020**, *14*, 491–506. [\[CrossRef\]](#)
- Dobrynin, M.; Murawski, J.; Baehr, J.; Ilyina, T. Detection and Attribution of Climate Change Signal in Ocean Wind Waves. *J. Clim.* **2015**, *28*, 1578–1591. [\[CrossRef\]](#)
- Wallemacq, P.; Rowena, H. *Economic Losses, Poverty and Disasters 1998–2017*; United Nations Office for Disaster Risk Reduction: Geneva, Switzerland, 2018.
- Grabemann, I.; Weisse, R. Climate Change Impact on Extreme Wave Conditions in the North Sea: An Ensemble Study. *Ocean Dyn.* **2008**, *58*, 199–212. [\[CrossRef\]](#)
- Hemer, M.A.; Fan, Y.; Mori, N.; Semedo, A.; Wang, X.L. Projected Changes in Wave Climate from a Multi-Model Ensemble. *Nat. Clim. Chang.* **2013**, *3*, 471–476. [\[CrossRef\]](#)
- Chowdhury, P.; Behera, M.R.; Reeve, D.E. Wave Climate Projections along the Indian Coast. *Int. J. Climatol.* **2019**, *39*, 4531–4542. [\[CrossRef\]](#)
- Mori, N.; Shimura, T.; Yasuda, T.; Mase, H. Multi-Model Climate Projections of Ocean Surface Variables under Different Climate Scenarios-Future Change of Waves, Sea Level and Wind. *Ocean Eng.* **2013**, *71*, 122–129. [\[CrossRef\]](#)
- Wang, X.L.; Feng, Y.; Swail, V.R. Changes in Global Ocean Wave Heights as Projected Using Multimodel CMIP5 Simulations. *Geophys. Res. Lett.* **2014**, *41*, 1026–1034. [\[CrossRef\]](#)
- Perez, J.; Menendez, M.; Camus, P.; Mendez, F.J.; Losada, I.J. Statistical Multi-Model Climate Projections of Surface Ocean Waves in Europe. *Ocean Model.* **2015**, *96*, 161–170. [\[CrossRef\]](#)
- Tebaldi, C.; Knutti, R. The Use of the Multi-Model Ensemble in Probabilistic Climate Projections. *Philos. Trans. R. Soc. A Math. Phys. Eng. Sci.* **2007**, *365*, 2053–2075. [\[CrossRef\]](#)
- Li, D.; Feng, J.; Xu, Z.; Yin, B.; Shi, H.; Qi, J. Statistical Bias Correction for Simulated Wind Speeds Over CORDEX-East Asia. *Earth Sp. Sci.* **2019**, *6*, 200–211. [\[CrossRef\]](#)
- Morim, J.; Hemer, M.; Andutta, F.; Shimura, T.; Cartwright, N. Skill and Uncertainty in Surface Wind Fields from General Circulation Models: Intercomparison of Bias between AGCM, AOGCM and ESM Global Simulations. *Int. J. Climatol.* **2020**, *40*, 2659–2673. [\[CrossRef\]](#)
- Diallo, I.; Sylla, M.B.; Giorgi, F.; Gaye, A.T.; Camara, M. Multimodel GCM-RCM Ensemble-Based Projections of Temperature and Precipitation over West Africa for the Early 21st Century. *Int. J. Geophys.* **2012**, *2012*, 972896. [\[CrossRef\]](#)
- Thober, S.; Samaniego, L. Robust Ensemble Selection by Multivariate Evaluation of Extreme Precipitation and Temperature Characteristics. *J. Geophys. Res.* **2014**, *119*, 594–613. [\[CrossRef\]](#)
- Kulkarni, S.; Deo, M.C.; Ghosh, S. Evaluation of Wind Extremes and Wind Potential under Changing Climate for Indian Offshore Using Ensemble of 10 GCMs. *Ocean Coast. Manag.* **2016**, *121*, 141–152. [\[CrossRef\]](#)
- Kumar, D.; Mishra, V.; Ganguly, A.R. Evaluating Wind Extremes in CMIP5 Climate Models. *Clim. Dyn.* **2015**, *45*, 441–453. [\[CrossRef\]](#)
- De Winter, R.C.; Sterl, A.; Ruessink, B.G. Wind Extremes in the North Sea Basin under Climate Change: An Ensemble Study of 12 CMIP5 GCMs. *J. Geophys. Res. Atmos.* **2013**, *118*, 1601–1612. [\[CrossRef\]](#)
- Bhat, S.; Jain, P.; Deo, M.C. Application of Regional Climate Models for Coastal Design Parameters along India. *J. Coast. Res.* **2018**, *35*, 110–121. [\[CrossRef\]](#)
- Chowdhury, P.; Behera, M.R. Evaluation of CMIP5 and CORDEX Derived Wave Climate in Indian Ocean. *Clim. Dyn.* **2018**, *52*, 4463–4482. [\[CrossRef\]](#)
- Perez, J.; Menendez, M.; Mendez, F.J.; Losada, I.J. Evaluating the Performance of CMIP3 and CMIP5 Global Climate Models over the North-East Atlantic Region. *Clim. Dyn.* **2014**, *43*, 2663–2680. [\[CrossRef\]](#)
- Mohan, S.; Bhaskaran, P.K. Evaluation of CMIP5 Climate Model Projections for Surface Wind Speed over the Indian Ocean Region. *Clim. Dyn.* **2019**, *53*, 5415–5435. [\[CrossRef\]](#)
- Krishnan, A.; Bhaskaran, P.K. Skill Assessment of Global Climate Model Wind Speed from CMIP5 and CMIP6 and Evaluation of Projections for the Bay of Bengal. *Clim. Dyn.* **2020**, *55*, 2667–2687. [\[CrossRef\]](#)
- Raju, K.S.; Kumar, D.N. Review of Approaches for Selection and Ensembling of GCMs. *J. Water Clim. Chang.* **2020**, *11*, 577–599. [\[CrossRef\]](#)
- Srinivasa Raju, K.; Nagesh Kumar, D. Ranking General Circulation Models for India Using TOPSIS. *J. Water Clim. Chang.* **2015**, *6*, 288–299. [\[CrossRef\]](#)
- Raju, K.S.; Kumar, D.N. Ranking of Global Climate Models for India Using Multicriterion Analysis. *Clim. Res.* **2014**, *60*, 103–117. [\[CrossRef\]](#)
- Saha, A.; Ghosh, S.; Sahana, A.S.; Rao, E.P. Failure of CMIP5 Climate Models in Simulating Post-1950 Decreasing Trend of Indian Monsoon. *Geophys. Res. Lett.* **2014**, *41*, 7323–7330. [\[CrossRef\]](#)
- Meher, J.K.; Das, L.; Akhter, J.; Benestad, R.E.; Mezghani, A. Performance of CMIP3 and CMIP5 GCMs to Simulate Observed Rainfall Characteristics over the Western Himalayan Region. *J. Clim.* **2017**, *30*, 7777–7799. [\[CrossRef\]](#)
- Rohini, P.; Rajeevan, M.; Mukhopadhyay, P. Future Projections of Heat Waves over India from CMIP5 Models. *Clim. Dyn.* **2019**, *53*, 975–988. [\[CrossRef\]](#)

29. Kumar, P.; Sarthi, P.P. Surface Temperature Evaluation and Future Projections Over India Using CMIP5 Models. *Pure Appl. Geophys.* **2019**, *176*, 5177–5201. [\[CrossRef\]](#)
30. Lyu, K.; Zhang, X.; Church, J.A.; Hu, J. Evaluation of the Interdecadal Variability of Sea Surface Temperature and Sea Level in the Pacific in CMIP3 and CMIP5 Models. *Int. J. Climatol.* **2016**, *36*, 3723–3740. [\[CrossRef\]](#)
31. Krishnan, A.; Bhaskaran, P.K. Performance of CMIP5 Wind Speed from Global Climate Models for the Bay of Bengal Region. *Int. J. Climatol.* **2020**, *40*, 3398–3416. [\[CrossRef\]](#)
32. Mohan, S.; Bhaskaran, P.K. Evaluation and Bias Correction of Global Climate Models in the CMIP5 over the Indian Ocean Region. *Environ. Monit. Assess.* **2019**, *191*, 806. [\[CrossRef\]](#) [\[PubMed\]](#)
33. Krishnan, A.; Bhaskaran, P.K. CMIP5 Wind Speed Comparison between Satellite Altimeter and Reanalysis Products for the Bay of Bengal. *Environ. Monit. Assess.* **2019**, *191*, 554. [\[CrossRef\]](#)
34. Barthelmie, R.J.; Pryor, S.C. Potential Contribution of Wind Energy to Climate Change Mitigation. *Nat. Clim. Chang.* **2014**, *4*, 684–688. [\[CrossRef\]](#)
35. Chaurasiya, P.K.; Warudkar, V.; Ahmed, S. Wind Energy Development and Policy in India: A Review. *Energy Strateg. Rev.* **2019**, *24*, 342–357. [\[CrossRef\]](#)
36. Yang, S.; Duan, S.; Fan, L.; Zheng, C.; Li, X.; Li, H.; Xu, J.; Wang, Q.; Feng, M. 10-Year Wind and Wave Energy Assessment in the North Indian Ocean. *Energies* **2019**, *12*, 3835. [\[CrossRef\]](#)
37. Irfan, M.; Zhao, Z.Y.; Mukeshimana, M.C.; Ahmad, M. Wind energy development in South Asia: Status, potential and policies. In Proceedings of the 2019 2nd International Conference on Computing, Mathematics and Engineering Technologies (iCoMET), Sukkur, Pakistan, 30–31 January 2019. [\[CrossRef\]](#)
38. Aboobacker, V.M.; Vethamony, P.; Rashmi, R. “Shamal” Swells in the Arabian Sea and Their Influence along the West Coast of India. *Geophys. Res. Lett.* **2011**, *38*, 1–7. [\[CrossRef\]](#)
39. Shanas, P.R.; Sanil Kumar, V. Temporal Variations in the Wind and Wave Climate at a Location in the Eastern Arabian Sea Based on ERA-Interim Reanalysis Data. *Nat. Hazards Earth Syst. Sci. Discuss.* **2013**, *1*, 7239–7269. [\[CrossRef\]](#)
40. Kumar, E.D.; Sannasiraj, S.A.; Sundar, V.; Polnikov, V.G. Wind-Wave Characteristics and Climate Variability in the Indian Ocean Region Using Altimeter Data. *Mar. Geod.* **2013**, *36*, 303–318. [\[CrossRef\]](#)
41. Anoop, T.R.; Kumar, V.S.; Shanas, P.R.; Johnson, G. Surface Wave Climatology and Its Variability in the North Indian Ocean Based on ERA-Interim Reanalysis. *J. Atmos. Ocean. Technol.* **2015**, *32*, 1372–1385. [\[CrossRef\]](#)
42. Kumar, V.S.; Joseph, J.; Amrutha, M.M.; Jena, B.K.; Sivakholundu, K.M.; Dubhashi, K.K. Seasonal and Interannual Changes of Significant Wave Height in Shelf Seas around India during 1998–2012 Based on Wave Hindcast. *Ocean Eng.* **2018**, *151*, 127–140. [\[CrossRef\]](#)
43. Zheng, C.W.; Pan, J.; Li, C.Y. Global Oceanic Wind Speed Trends. *Ocean Coast. Manag.* **2016**, *129*, 15–24. [\[CrossRef\]](#)
44. Yang, S.; Li, Z.; Yu, J.Y.; Hu, X.; Dong, W.; He, S. El Niño–Southern Oscillation and Its Impact in the Changing Climate. *Natl. Sci. Rev.* **2018**, *5*, 840–857. [\[CrossRef\]](#)
45. Sinha, M.; Jha, S.; Chakraborty, P. Indian Ocean Wind Speed Variability and Global Teleconnection Patterns. *Oceanologia* **2020**, *62*, 126–138. [\[CrossRef\]](#)
46. Xie, S.P.; Deser, C.; Vecchi, G.A.; Collins, M.; Delworth, T.L.; Hall, A.; Hawkins, E.; Johnson, N.C.; Cassou, C.; Giannini, A.; et al. Towards Predictive Understanding of Regional Climate Change. *Nat. Clim. Chang.* **2015**, *5*, 921–930. [\[CrossRef\]](#)
47. Seemanth, M.; Bhowmick, S.A.; Kumar, R.; Sharma, R. Sensitivity Analysis of Dissipation Parameterizations in a Third-Generation Spectral Wave Model, WAVEWATCH III for Indian Ocean. *Ocean Eng.* **2016**, *124*, 252–273. [\[CrossRef\]](#)
48. Wu, L.; Qin, J.; Wu, T.; Li, X. Trends in Global Ocean Surface Wave Characteristics as Represented in the ERA-Interim Wave Reanalysis for 1979–2010. *J. Mar. Sci. Technol.* **2018**, *23*, 2–9. [\[CrossRef\]](#)
49. Wang, X.L.; Swail, V.R.; Cox, A. Dynamical versus Statistical Downscaling Methods for Ocean Wave Heights. *Int. J. Climatol.* **2009**, *30*, 317–332. [\[CrossRef\]](#)
50. Jain, P.; Deo, M.C. Climate change impact on design waves using climate models. In Proceedings of the Fourth International Conference in Ocean Engineering (ICOE2018); Murali, K., Sriram, V., Samad, A., Saha, N., Eds.; Springer Singapore: Singapore, 2019; pp. 783–794.
51. Muhammed Naseef, T.; Sanil Kumar, V. Climatology and Trends of the Indian Ocean Surface Waves Based on 39-Year Long ERA5 Reanalysis Data. *Int. J. Climatol.* **2019**, *40*, 979–1006. [\[CrossRef\]](#)
52. Kulkarni, S.; Deo, M.C.; Ghosh, S. Performance of the CORDEX Regional Climate Models in Simulating Offshore Wind and Wind Potential. *Theor. Appl. Climatol.* **2018**, *135*, 1449–1464. [\[CrossRef\]](#)
53. Parker, K.; Hill, D.F. Evaluation of Bias Correction Methods for Wave Modeling Output. *Ocean Model.* **2017**, *110*, 52–65. [\[CrossRef\]](#)
54. Li, H.; Sheffield, J.; Wood, E.F. Bias Correction of Monthly Precipitation and Temperature Fields from Intergovernmental Panel on Climate Change AR4 Models Using Equidistant Quantile Matching. *J. Geophys. Res. Atmos.* **2010**, *115*, D10. [\[CrossRef\]](#)
55. Perkins, S.E.; Pitman, A.J.; Holbrook, N.J.; McAneney, J. Evaluation of the AR4 Climate Models’ Simulated Daily Maximum Temperature, Minimum Temperature, and Precipitation over Australia Using Probability Density Functions. *J. Clim.* **2007**, *20*, 4356–4376. [\[CrossRef\]](#)
56. Kendall, M.G. Rank Correlation Methods. *Biometrika* **1957**, *44*, 107–116. [\[CrossRef\]](#)
57. Mann, H.B. Non-Parametric Test Against Trend. *Econometrica* **1945**, *13*, 245–259. [\[CrossRef\]](#)
58. Sen, P.K. Estimates of the Regression Coefficient Based on Kendall’s Tau. *J. Am. Stat. Assoc.* **1968**, *63*, 1379–1389. [\[CrossRef\]](#)

59. Kulkarni, A.; Von Storch, H. Monte Carlo Experiments on the Effect of Serial Correlation on the Mann-Kendall Test of Trend. *Meteorol. Z.* **1995**, *4*, 82–85. [[CrossRef](#)]
60. Yue, S.; Wang, C.Y. Applicability of Prewhitening to Eliminate the Influence of Serial Correlation on the Mann-Kendall Test. *Water Resour. Res.* **2002**, *38*, 1–4. [[CrossRef](#)]
61. Wang, F.; Shao, W.; Yu, H.; Kan, G.; He, X.; Zhang, D.; Ren, M.; Wang, G. Re-Evaluation of the Power of the Mann-Kendall Test for Detecting Monotonic Trends in Hydrometeorological Time Series. *Front. Earth Sci.* **2020**, *8*, 1–12. [[CrossRef](#)]
62. Stouffer, R.J.; Eyring, V.; Meehl, G.A.; Bony, S.; Senior, C.; Stevens, B.; Taylor, K.E. CMIP5 Scientific Gaps and Recommendations for CMIP6. *Bull. Am. Meteorol. Soc.* **2017**, *98*, 95–105. [[CrossRef](#)]
63. Müller, W.A.; Jungclaus, J.H.; Mauritsen, T.; Baehr, J.; Bittner, M.; Budich, R.; Bunzel, F.; Esch, M.; Ghosh, R.; Haak, H.; et al. A Higher-Resolution Version of the Max Planck Institute Earth System Model (MPI-ESM1.2-HR). *J. Adv. Model. Earth Syst.* **2018**, *10*, 1383–1413. [[CrossRef](#)]
64. Dix, M.; Vohralik, P.; Bi, D.; Rashid, H.; Marsland, S.; O’Farrell, S.; Uotila, P.; Hirst, T.; Kowalczyk, E.; Sullivan, A.; et al. The ACCESS Coupled Model: Documentation of Core CMIP5 Simulations and Initial Results. *Aust. Meteorol. Oceanogr. J.* **2013**, *63*, 83–99. [[CrossRef](#)]
65. Bi, D.; Dix, M.; Marsland, S.J.; O’Farrell, S.; Rashid, H.; Uotila, P.; Hirst, A.C.; Kowalczyk, E.; Golebiewski, M.; Sullivan, A.; et al. The ACCESS Coupled Model: Description, Control Climate and Preliminary Validation. *Aust. Meteorol. Oceanogr. J.* **2013**, *63*, 41–64. [[CrossRef](#)]
66. Zha, J.; Wu, J.; Zhao, D.; Fan, W. Future Projections of the Near-Surface Wind Speed over Eastern China Based on CMIP5 Datasets. *Clim. Dyn.* **2020**, *54*, 2361–2385. [[CrossRef](#)]
67. Chylek, P.; Li, J.; Dubey, M.; Wang, M. Observed and Model Simulated 20th Century Arctic Temperature Variability: Canadian Earth System Model CanESM2. *Atmos. Chem. Phys. Discuss.* **2011**, *11*, 22893–22907. [[CrossRef](#)]
68. Martin, G.M.; Bellouin, N.; Collins, W.J.; Culverwell, I.D.; Halloran, P.R.; Hardiman, S.C.; Hinton, T.J.; Jones, C.D.; McDonald, R.E.; McLaren, A.J.; et al. The HadGEM2 Family of Met Office Unified Model Climate Configurations. *Geosci. Model Dev.* **2011**, *4*, 723–757. [[CrossRef](#)]
69. Watanabe, S.; Hajima, T.; Sudo, K.; Nagashima, T.; Takemura, T.; Okajima, H.; Nozawa, T.; Kawase, H.; Abe, M.; Yokohata, T.; et al. MIROC-ESM 2010: Model Description and Basic Results of CMIP5-20c3m Experiments. *Geosci. Model Dev.* **2011**, *4*, 845–872. [[CrossRef](#)]
70. Collins, W.J.; Bellouin, N.; Doutriaux-Boucher, M.; Gedney, N.; Halloran, P.; Hinton, T.; Hughes, J.; Jones, C.D.; Joshi, M.; Liddicoat, S.; et al. Development and Evaluation of an Earth-System Model—HadGEM2. *Geosci. Model Dev.* **2011**, *4*, 1051–1075. [[CrossRef](#)]
71. Dunne, J.P.; John, J.G.; Shevliakova, S.; Stouffer, R.J.; Krasting, J.P.; Malyshev, S.L.; Milly, P.C.D.; Sentman, L.T.; Adcroft, A.J.; Cooke, W.; et al. GFDL’s ESM2 Global Coupled Climate-Carbon Earth System Models. Part II: Carbon System Formulation and Baseline Simulation Characteristics. *J. Clim.* **2013**, *26*, 2247–2267. [[CrossRef](#)]
72. Dunne, J.P.; John, J.G.; Adcroft, A.J.; Griffies, S.M.; Hallberg, R.W.; Shevliakova, E.; Stouffer, R.J.; Cooke, W.; Dunne, K.A.; Harrison, M.J.; et al. GFDL’s ESM2 Global Coupled Climate-Carbon Earth System Models. Part I: Physical Formulation and Baseline Simulation Characteristics. *J. Clim.* **2012**, *25*, 6646–6665. [[CrossRef](#)]
73. Dufresne, J.L.; Foujols, M.A.; Denvil, S.; Caubel, A.; Marti, O.; Aumont, O.; Balkanski, Y.; Bekki, S.; Bellenger, H.; Benshila, R.; et al. Climate Change Projections Using the IPSL-CM5 Earth System Model: From CMIP3 to CMIP5. *Clim. Dyn.* **2013**, *40*, 2123–2165. [[CrossRef](#)]
74. Boucher, O.; Servonnat, J.; Albright, A.L.; Aumont, O.; Balkanski, Y.; Bastrikov, V.; Bekki, S.; Bonnet, R.; Bony, S.; Bopp, L.; et al. Presentation and Evaluation of the IPSL-CM6A-LR Climate Model. *J. Adv. Model. Earth Syst.* **2020**, *12*, 1–52. [[CrossRef](#)]
75. Thomson, A.M.; Calvin, K.V.; Smith, S.J.; Kyle, G.P.; Volke, A.; Patel, P.; Delgado-Arias, S.; Bond-Lamberty, B.; Wise, M.A.; Clarke, L.E.; et al. RCP4.5: A Pathway for Stabilization of Radiative Forcing by 2100. *Clim. Change* **2011**, *109*, 77–94. [[CrossRef](#)]
76. Rogelj, J.; Meinshausen, M.; Knutti, R. Global Warming under Old and New Scenarios Using IPCC Climate Sensitivity Range Estimates. *Nat. Clim. Chang.* **2012**, *2*, 248–253. [[CrossRef](#)]